

# Biophysically grounded mean-field models of neural populations under electrical stimulation

Caglar Cakan<sup>1,2,\*</sup> and Klaus Obermayer<sup>1,2</sup>

<sup>1</sup>Department of Software Engineering and Theoretical Computer Science, Technische Universität Berlin, Germany

<sup>2</sup>Bernstein Center for Computational Neuroscience Berlin, Germany

\*cakan@ni.tu-berlin.de

## ABSTRACT

Electrical stimulation of large neural networks is a key tool for understanding neural population dynamics and ultimately for developing clinical treatments. However, computational models of cortical networks of spiking neurons are inherently hard to simulate and analyze. We present an efficient mean-field model of excitatory and inhibitory adaptive exponential integrate-and-fire (AdEx) neurons of which we analyse the dynamical properties and validate the results using detailed network simulations. Bifurcation diagrams reflecting the network's state reveal asynchronous up and down-states, bistable regimes, and oscillatory regions corresponding to fast excitation-inhibition and slow excitation-adaptation feedback loops. In this dynamical landscape, electrical stimuli can cause state transitions, such as turning on and off oscillations. Oscillatory input can frequency-entrain and phase-lock endogenous oscillations. The effects of time-varying external stimulation are well-predicted by the mean-field model, further underpinning the utility of low-dimensional neural mass models.

## Introduction

A paradigm which has proven to be successful in physical sciences is to systematically perturb a system in order to uncover its dynamical properties. This has also worked well for the different scales at which neural systems are studied. Mapping input responses experimentally has been key in uncovering the dynamical repertoire of single neurons<sup>1,2</sup> and large neural populations such as cortical slice preparations<sup>3</sup>. It has been repeatedly shown that non-invasive brain stimulation can modulate oscillations of ongoing brain activity<sup>4,5</sup> and brain function<sup>6,7</sup> and has enabled a new way for treatment of clinical disorders such as epilepsy<sup>8</sup>. Moreover, electrical input to neural populations can also originate from the active neural tissue itself, causing endogenous (intrinsic) extracellular electric fields which modulate neural activity<sup>10,11</sup>.

However, a complete understanding of how electrical stimulation affects large networks of neurons remains elusive. For this reason, we present a computational framework and tools for studying the interaction of time-varying electric inputs with the dynamics of large neural populations. Unlike *in vivo* and *in vitro* experimental setups, *in silico* models of electrical stimulation offer the possibility to study a wide range of neuronal and stimulation parameters and might help to interpret experimental results.

For analytical tractability, theoretical research of the effects of electrical stimulation has relied on the use of mean-field methods to derive low-dimensional neural mass models<sup>16–19</sup>. Instead of simulating a large number of neurons, these models aim to approximate the population dynamics of interconnected neurons by means of dimensionality reduction. At the cost of disregarding the dynamics of individual neurons, it is possible to make statistical assumptions about large random neural networks and approximate their macroscopic behavior, such as the mean firing rate of the population.

Analyzing the state space of mean-field models has helped to characterize the dynamical states of coupled neuronal populations<sup>20,21</sup>. Due to their computational efficiency, mean-field neural mass models are also typically used in whole-brain network models<sup>22,23</sup>, where they represent individual brain areas. This made it possible to study the effects of external electrical stimulation on the ongoing activity of the human brain on a system level<sup>24,25</sup>.

Naturally, neural population models have to strike a balance between analytical tractability, computational cost, and biophysical realism. Thus, relating predictions from mean-field models to networks of biophysically realistic spiking neural populations is a challenging task. In order to bridge this gap, we present a mean-field population model based on a linear-nonlinear cascade<sup>26,27</sup> of a large network of spiking adaptive exponential (AdEx) integrate-and-fire neurons<sup>28</sup>. The AdEx model neuron in particular quite successfully reproduces the sub- and supra-threshold voltage traces of single pyramidal neurons found in cerebral cortex<sup>29,30</sup> while offering the advantage of having interpretable biophysical parameters. In our mean-field approximation, the parameters that define its state space of the population are directly related to the biophysical parameters of the network of AdEx neurons.

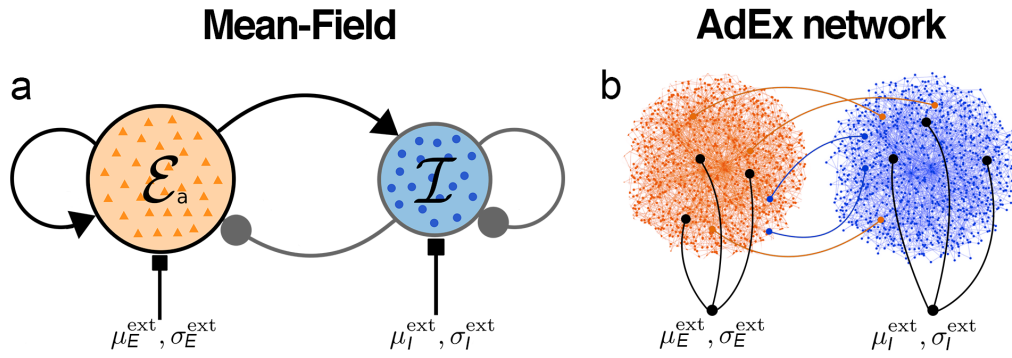


**Figure 1. Schematic of the cortical motif.** Coupled populations of excitatory (red) and inhibitory (blue) neurons. **(a)** Mean-field neural mass model with axonal feedforward and feedback connections. Each node represents a population. **(b)** Schematic of the corresponding spiking AdEx neuron network with connections between and within both populations. Both populations receive independent input currents with a mean  $\mu_{\alpha}^{\text{ext}}$  and a standard deviation  $\sigma_{\alpha}^{\text{ext}}$  across all neurons of population  $\alpha \in \{E, I\}$ .

In the following, we consider a classical motif of two delay-coupled populations of excitatory and inhibitory neurons that represents a cortical neural mass (Fig. 1). We explore the rich dynamical landscape of this generic setup and investigate the effects of slow somatic adaptation currents on the population dynamics. We then apply time-varying electrical input currents to the excitatory population and observe frequency and amplitude-dependent effects of the interactions between stimulus and endogenous oscillations of the system. We estimate the equivalent *extracellular electric field* amplitudes corresponding to these effects using previous results<sup>31</sup> of a spatially extended neuron model with a passive dendritic cable.

Predictions from mean-field theory are validated using simulations of large spiking neural networks. A close relationship of the mean-field model to the ground-truth model is established, proving its practical and theoretical utility. The mean-field model retains all dynamical states of the large network of individual neurons and predicts the interaction of the system with external electrical stimulation to a remarkable degree. We believe that our results can help to understand the rich and plentiful observations in real neural systems subject to external stimulation and may provide a useful tool for studying the effects on the population activity.

## Results

### The cortical mass model

Here we study a cortical mass model which consists of two populations of excitatory adaptive (E) and inhibitory (I) exponential integrate-and-fire (AdEx) neurons (Fig. 1). Both populations are delay-coupled and the excitatory population has a somatic adaptation feedback mechanism. The low-dimensional mean-field model (Fig. 1 a) is derived from the large network of spiking AdEx neurons (Fig. 1 b).

For the construction of the mean-field model, a set of conditions need to be fulfilled: We assume the number of neurons to be very large, all neurons within a population to have equal properties, and the connectivity between neurons to be sparse and random. Additional assumptions about the mathematical nature and a detailed derivation of the mean-field model is presented in the Methods.

### Bifurcation diagrams: a map of the dynamical landscape

The E-I motif shown in Fig. 1 can occupy various network states, depending on the baseline inputs to both populations. By gradually changing the inputs, we map out the state space of the system, depicted in the bifurcation diagrams in Fig. 2. Small changes of the parameters of a nonlinear system can cause sudden and dramatic changes of its overall behavior, called bifurcations. Bifurcations separate the state space into distinct regions of network states between which the system can transition from one to the other. In our case, the dynamical state of the E-I system depends on external inputs to both subpopulations, which are directly affected by external electrical stimulation and other driving sources, e.g. inputs from other neural populations such as other brain regions.

Comparing the bifurcation diagrams of the mean-field model (Figs. 2 a, c) to the ground truth spiking AdEx network (Figs. 2 b, d) demonstrates the similarity between both dynamical landscapes. Transitions between states take place at comparable baseline input values and in a well-preserved order.

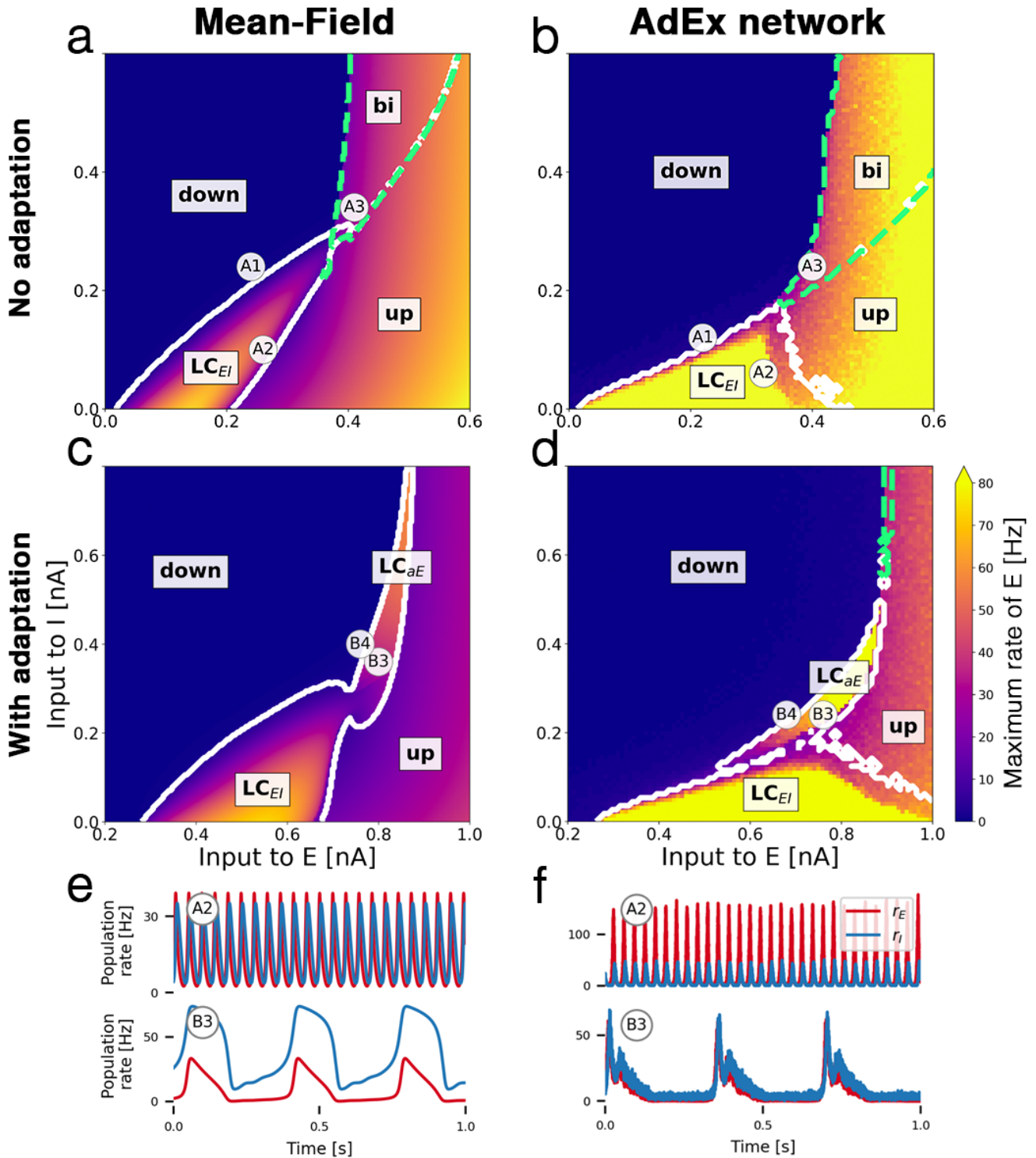


**Figure 2. Bifurcation diagrams and time series.** Bifurcation diagrams a-d depict the state space of the E-I system in terms of the mean external input currents  $C \cdot \mu_{\alpha}^{\text{ext}}$  to both subpopulations  $\alpha \in \{E, I\}$ . (a) Bifurcation diagram of mean-field model without adaptation with *up* and *down*-states, a bistable region *bi* (green dashed contour) and an oscillatory region  $LC_{EI}$  (white solid contour). (b) Diagram of the corresponding AdEx network. (c) Mean-field model with somatic adaptation. The bistable region is replaced by a slow oscillatory region  $LC_{aE}$ . (d) Diagram of the corresponding AdEx network. The color in panels a-d indicate the maximum population rate of the excitatory population (clipped at 80 Hz). (e) Example time series of the population rates of excitatory (red) and inhibitory (blue) populations at point A2 (top row) which is located in the fast excitatory-inhibitory limit cycle  $LC_{EI}$ , and at point B3 (bottom row) which is located in the slow limit cycle  $LC_{aE}$ . (f) Time series at corresponding points for the AdEx network. All parameters are listed in Table 1. The mean input currents to the points of interests A1-A3 and B1-B4 are provided in Table 2.

Since the space of possible biophysical parameter configurations is vast, we focus on two variants of the model: one without a somatic adaptation mechanism, Figs. 2 a and b, and one with finite sub-threshold and spike-triggered adaptation in Figs. 2 c and d. Both variants feature distinct states and dynamics.

### **Bistable up- and down-states without adaptation**

Figures 2 a and b show the bifurcation diagrams of the E-I system without somatic adaptation. There are two stable fixed-point solutions of the system with a constant firing rate: a low-activity *down-state* and a high-activity *up-state*. These macroscopic states correspond to asynchronous firing activity on a microscopic level<sup>16</sup>. In accordance with previous studies<sup>32</sup>, at larger mean background input currents, there is a *bistable* region in which the *up-state* and the *down-state* coexist. At smaller mean input values, the recurrent coupling of excitatory and inhibitory neurons gives rise to an oscillatory limit cycle  $LC_{EI}$  with an alternating activity between the two populations. Example time series of the population rates of E and I inside the limit cycle are shown in Figs. 2 e and f (top row). The frequency inside the oscillatory region depends on the inputs to both populations and ranges from 8 Hz to 29 Hz in the mean-field model and from 4 Hz to 44 Hz in the AdEx network for the parameters given (see Supplementary Fig. 11).

All macroscopic network states of the AdEx network are represented in the mean-field model. The bifurcation line that marks the transition from the *down-state* to  $LC_{EI}$  appears at a similar location in the state space, close to the diagonal at which the mean inputs to E and I are equal, in both, the mean-field and the spiking network model. However, the shape and width of the oscillatory region, as well as the amplitudes and frequencies of the oscillations differ. In Figs. 2 e and f (top row), the differences are due to the location of the selected points B2 in the bifurcation diagrams, which are not particularly chosen to precisely match each other in amplitude or frequency but rather in the approximate location in the state space. Overall, the AdEx network exhibits larger amplitudes across the oscillatory regime and the excitatory amplitudes are larger than the inhibitory amplitudes (Supplementary Fig. 9). Another notable difference is the small bistable overlap of the *up-state* region with the oscillatory region  $LC_{EI}$  in the mean-field model (Fig. 2 a) which could not be observed in the AdEx network.

### **Somatic adaptation causes slow oscillations**

In Figs. 2 c and d, bifurcation diagrams of the system with somatic adaptation are shown. Compared to Figs. 2 a and b (without adaptation), the state space, including the oscillatory region  $LC_{EI}$ , is shifted to the right, meaning that larger excitatory input currents are necessary to compensate for the inhibiting sub-threshold adaptation currents. The main effect that is caused by adaptation is the appearance of a slow oscillatory region labeled  $LC_{aE}$  in Figs. 2 c and d. The reason for the emergence of this oscillation is the destabilizing effect the inhibiting adaptation currents have on the *up-state* inside the *bistable* region<sup>33</sup>. As the mean adaptation current builds up due to high population firing rate, the *up-state* "decays" and transitions to the *down-state*. The resulting low activity causes a decrease of the adaptation currents which in turn allow the activity to increase back into the *up-state*, resulting in a slow oscillation. These low-frequency oscillations range from 0.5 Hz to 5 Hz for the parameters given.

The bifurcation diagrams in Fig. 3 show how the emergence of the slow oscillation depends on the adaptation mechanism. Increasing the subthreshold adaptation parameter primarily shifts the state space to the right whereas a larger spike-triggered adaptation parameter value enlarges oscillatory regions. Both parameters cause the *bistable* region to shrink until it is eventually replaced by a slow oscillatory region  $LC_{aE}$ . Again, the state space of the mean-field model (3 a) reflects the AdEx network (3 b) accurately.

### **Time-varying stimulation and electric field effects**

To describe the time-dependent properties of the system, we study the effects of time-varying external stimulation and the interactions with ongoing oscillatory states. External stimulation is implemented by coupling an electric input current to the excitatory population. This additional input current may be a result of an externally applied electric field or synaptic input from other neural populations. For the cases without adaptation, we can calculate an equivalent extracellular electric field strength that correspond to the effects of an input current (see Methods).

Since due to the presence of apical dendrites excitatory neurons in the neocortex are most susceptible to electric fields<sup>34</sup>, only time-varying input to the excitatory population is studied. This choice is also motivated in the context of inter-areal brain network models where connections between brain areas are usually considered between excitatory subpopulations.

Given the multitude of possible states of the system, its response to external input critically depends on the dynamical landscape around its current state. It is important to keep in mind that the bifurcation diagrams (Figs. 2 and 3) are valid only for constant external input currents. However, they provide helpful insights about the dynamics of the non-stationary system assuming that the bifurcation diagrams do not change too much as we vary the input parameter  $\mu_e^{ext}(t)$  over time.

Figs. 4 a-f show how a step current input pushes the system in and out of specific states of the E-I system. A positive step current represents a movement in positive direction of the  $\mu_e^{ext}$  axis in Fig. 2. Figs. 4 a and b show input-driven transitions from the low-activity *down-state* into the fast oscillatory limit cycle  $LC_{EI}$ . Similar behavior can be observed in Figs. 4 c and d where

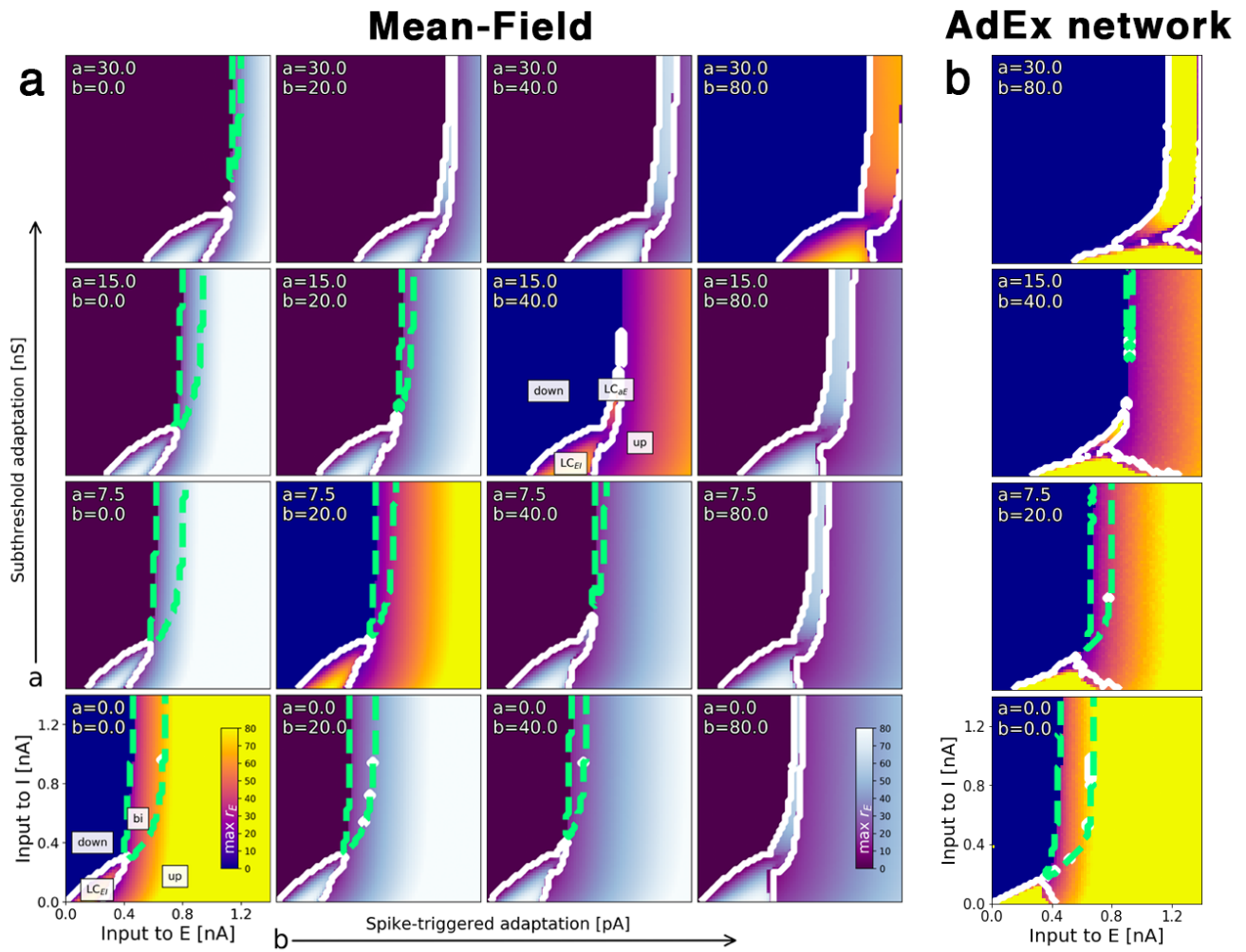


**Figure 3. Transition from multistability to slow oscillation is caused by somatic adaptation.** Bifurcation diagrams depending on the external input current  $C \cdot \mu_{\alpha}^{\text{ext}}$  to both populations  $\alpha \in \{E, I\}$  for varying somatic adaptation parameters  $a$  and  $b$ . Color indicates maximum rate of the excitatory population. Oscillatory regions have a white contour, bistable regions have a green dashed contour. **(a)** Bifurcation diagrams of the mean-field model. On the diagonal (bright-colored diagrams), adaptation parameters coincide with **(b)**. **(b)** Bifurcation diagrams of the corresponding AdEx network. All parameters are listed in Table 1.



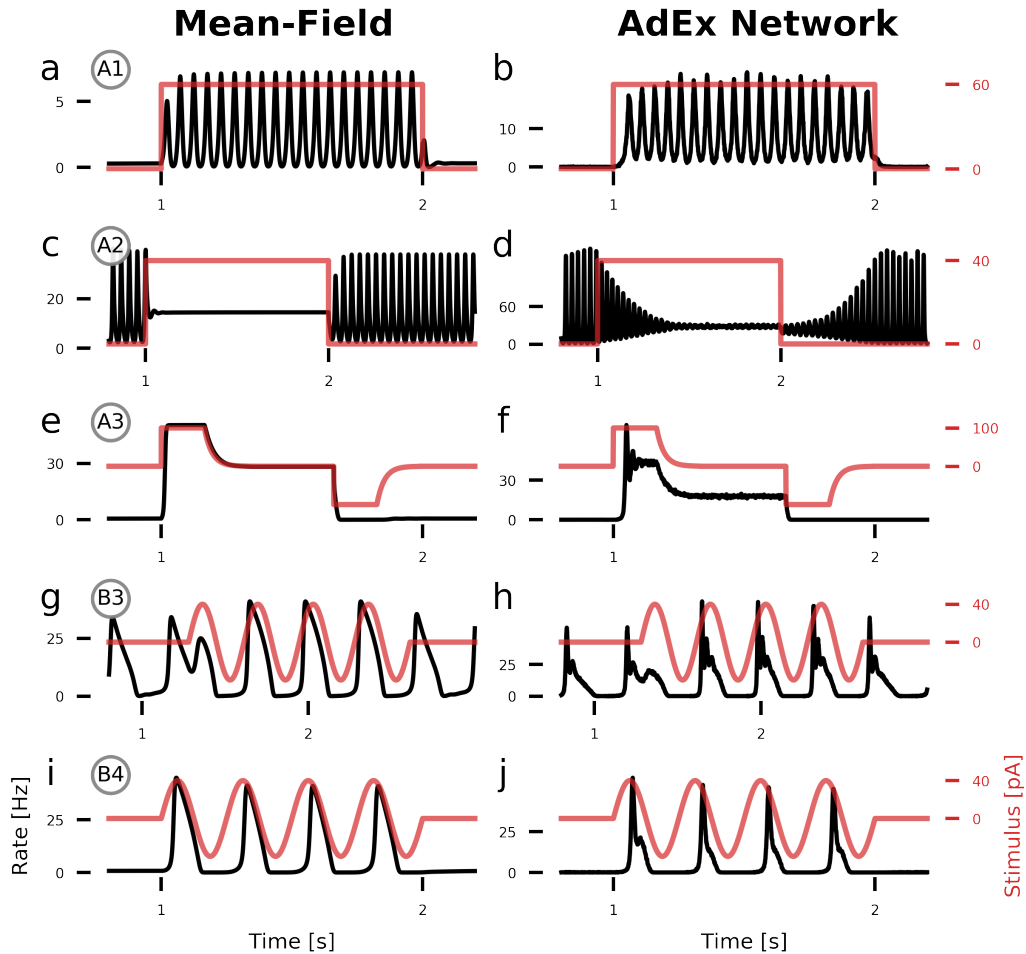


**Figure 4. State-dependent population response to time-varying input currents.** Population rates of the excitatory population (black) with an additional external electrical stimulus (red) applied to the excitatory population. **(a, b)** A DC step input with amplitude 60 pA (equivalent E-field amplitude: 12 V/m) pushes the system from the low-activity fixed point into the fast limit cycle  $LC_{EI}$ . **(c, d)** A step input with amplitude 40 pA (8 V/m) pushes the system from  $LC_{EI}$  into the *up-state*. **(e, f)** In the multistable region *bi*, a step input with amplitude 100 pA (20 V/m) pushes the system from the *down-state* into the *up-state* and back. **(g, h)** Inside the slow oscillatory region  $LC_{aE}$ , an oscillating input current with amplitude 40 pA and a (frequency-matched) frequency of 3 Hz phase-locks the ongoing oscillation. **(i, j)** A slow 4 Hz oscillatory input with amplitude 40 pA drives oscillations if the system is close to the oscillatory region  $LC_{aE}$ . All parameters are given in Table 1, the parameters of the points of interest are given in Table 2.

we push the system's state from  $LC_{EI}$  into the *up-state*, effectively being able to turn oscillations on and off with a direct input current. The time it takes to transition between states is longer for the AdEx network.

Inside the *bistable* region, we can use the hysteresis effect to transition between the *down-state* and the *up-state* and vice versa. After application of an initial push in the desired direction, the system remains in that state, reflecting the system's bistable nature.

When adaptation is turned on, a slow oscillatory input current can entrain the ongoing oscillation. In Figs. 4 g and h, the oscillation is initially out of phase with the external input but is quickly phase-locked. Placed close to the boundary of the slow oscillatory region  $LC_{aE}$ , in Figs. 4 i and j we show how an oscillatory input with a similar frequency as the limit cycle periodically drives the system from the *down-state* into one oscillation period.

### **Frequency entrainment with oscillatory input**

To study the frequency-dependent response of the E-I system, we vary the amplitude and frequency of an oscillatory input to the excitatory population (Fig. 5). The unperturbed system is parameterized to be in the fast limit cycle  $LC_{EI}$  with its endogenous frequency  $f_0$ .

The external stimulus with frequency  $f_{ext}$  entrains the ongoing oscillation in a range around  $f_0$ , the resonant frequency of the system. Here, the ongoing oscillation essentially follows the external drive and adjusts its frequency to it (Fig. 5 a). A second (narrower) range of frequency entrainment appears as  $f_{ext}$  approaches  $2f_0$ , representing the ability of the input to entrain oscillations at half of its frequency. Due to interference of the frequencies of ongoing and external oscillations, the spectrum has peaks at the difference of both frequencies which appear as X-shaped patterns in the frequency diagrams. The AdEx neuron network shows a similar behavior (Fig. 5 b), albeit the range of entrainment is smaller than in the mean-field model, despite the stimulation amplitude being twice as large.

For a stronger mean input current, the range of frequency entrainment is widened considerably. In Fig. 5 c, the input dominates the spectrum at very low frequencies. The peak of the spectrum reverts back to approximately  $f_0$  if the external frequency  $f_{ext}$  is close to the first harmonic  $2f_0$  of the endogenous frequency. We see multiple lines emerging in the frequency spectra that correspond to the harmonics and subharmonics of the external frequency and its interaction with the endogenous frequency  $f_0$ , creating a complex pattern in the diagrams. In the case of the AdEx network in Fig. 5 d, the interaction patterns of the entrained harmonics with the endogenous oscillation are similar but the endogenous oscillation is able to sustain itself better, visible as horizontal lines in the diagram. This is due to the overall weaker susceptibility to external input of the AdEx network compared to the mean-field model.

Overall, there is a good qualitative agreement of the frequency spectra of both models, reflecting that interactions of external input and ongoing oscillations are well-captured by the mean-field model.

### **Phase locking with oscillatory input**

Here we quantify the ability of an oscillating external input current to the excitatory population to synchronize an ongoing oscillation to itself if both frequencies, the driver and the endogenous frequency, are close to each other (frequency matching). An example time series of a stimulus entraining an ongoing slow oscillation is shown in Fig. 4 h.

In Fig. 6, we find phase locking by measuring the time course of the phase difference between the stimulus and the population rate. If phase locking is successful the phase difference remains constant. In Fig. 6 a, the region of phase locking for an external input of frequency  $f_{ext}$  is centered around the endogenous frequency  $f_0$  of the unperturbed system. Increasing the stimulus amplitude widens the range around  $f_0$  at which phase locking is effective. An example time series of successful phase locking inside this region is shown in Fig 6 c. If the input is not able to phase-lock the ongoing activity, a small difference between the driver frequency  $f_{ext}$  and  $f_0$  can cause a slow beating of the activity with a frequency of roughly the difference  $|f_{ext} - f_0|$ . Thus, a small frequency mismatch can produce a very slowly oscillating activity (Fig. 6 c at points 2-4). Figure 6 d at point 2 shows the same drifting effect in the AdEx network. Due to finite-size noise in the AdEx neuron network, an irregular switching between synchrony and asynchrony can be observed at the edges of the phase locking region in Fig. 6 d at point 3. Compared to the mean-field model, the frequency of the beating activity in the AdEx network is less regular (Fig. 6 d at point 4).

In the phase locking diagrams Figs. 6 a and b, the equivalent external electric field amplitudes are shown. Small amplitudes (0.5 V/m for the mean-field model, 1 V/m - 2 V/m for the AdEx network) are able to phase-lock the ongoing oscillations if the frequencies roughly match.

## **Discussion**

In this paper we explored the dynamical properties of a cortical neural mass model of excitatory and inhibitory (E-I) adaptive exponential integrate-and-fire (AdEx) neurons by studying their response to external electrical stimulation. Results from a low-dimensional mean-field model of the spiking AdEx neuron network were compared with large network simulations (Fig.

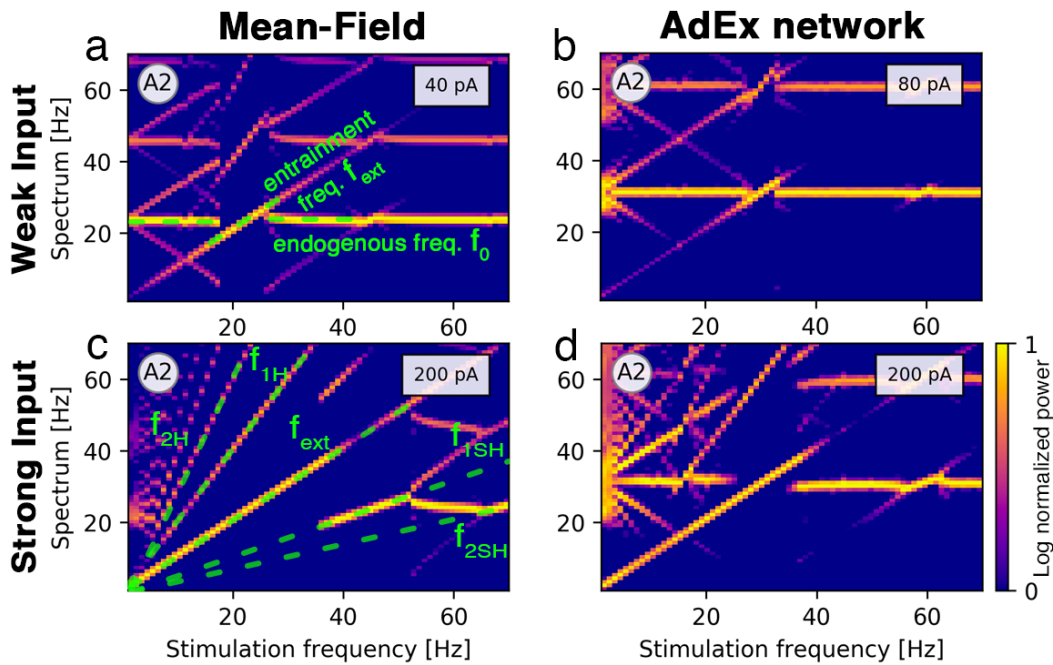


**Figure 5. Frequency entrainment of the population activity in response to oscillatory input.** The color represents the log-normalized power of the excitatory population's rate frequency spectrum with high power in bright yellow and low power in dark purple. **(a)** Spectrum of mean-field model parameterized at point A2 with an ongoing oscillation frequency of  $f_0 = 22$  Hz (horizontal green dashed line) in response to a stimulus with increasing frequency and an amplitude of 40 pA. An external electric field with a resonant stimulation frequency of  $f_0$  has an equivalent strength of 3 V/m. The stimulus entrains the oscillation from 18 Hz to 26 Hz, represented by a dashed green diagonal line. At 27 Hz, the oscillation falls back to its original frequency  $f_0$ . At a stimulation frequency of  $2f_0$ , the ongoing oscillation at  $f_0$  locks again to the stimulus in a smaller range from 43 Hz to 47 Hz. **(b)** AdEx network with  $f_0 = 30$  Hz. Entrainment with an input current of 80 pA is effective from 27 Hz to 33 Hz. Electric field amplitude with frequency  $f_0$  corresponds to 5 V/m. **(c)** Mean-field model with a stimulus amplitude of 200 pA. Green dashed lines mark the driving frequency  $f_{ext}$  and its first and second harmonics  $f_{1H}$  and  $f_{2H}$  and subharmonics  $f_{1SH}$  and  $f_{2SH}$ . Entrained is now effective at the lowest stimulation frequencies until at 36 Hz the oscillation falls back to a frequency of 20 Hz. New diagonal lines appear due to interactions of the endogenous oscillation with the entrained harmonics and subharmonics. **(d)** AdEx network with stimulation amplitude of 240 pA. All parameters are given in Tables 1 and 2.



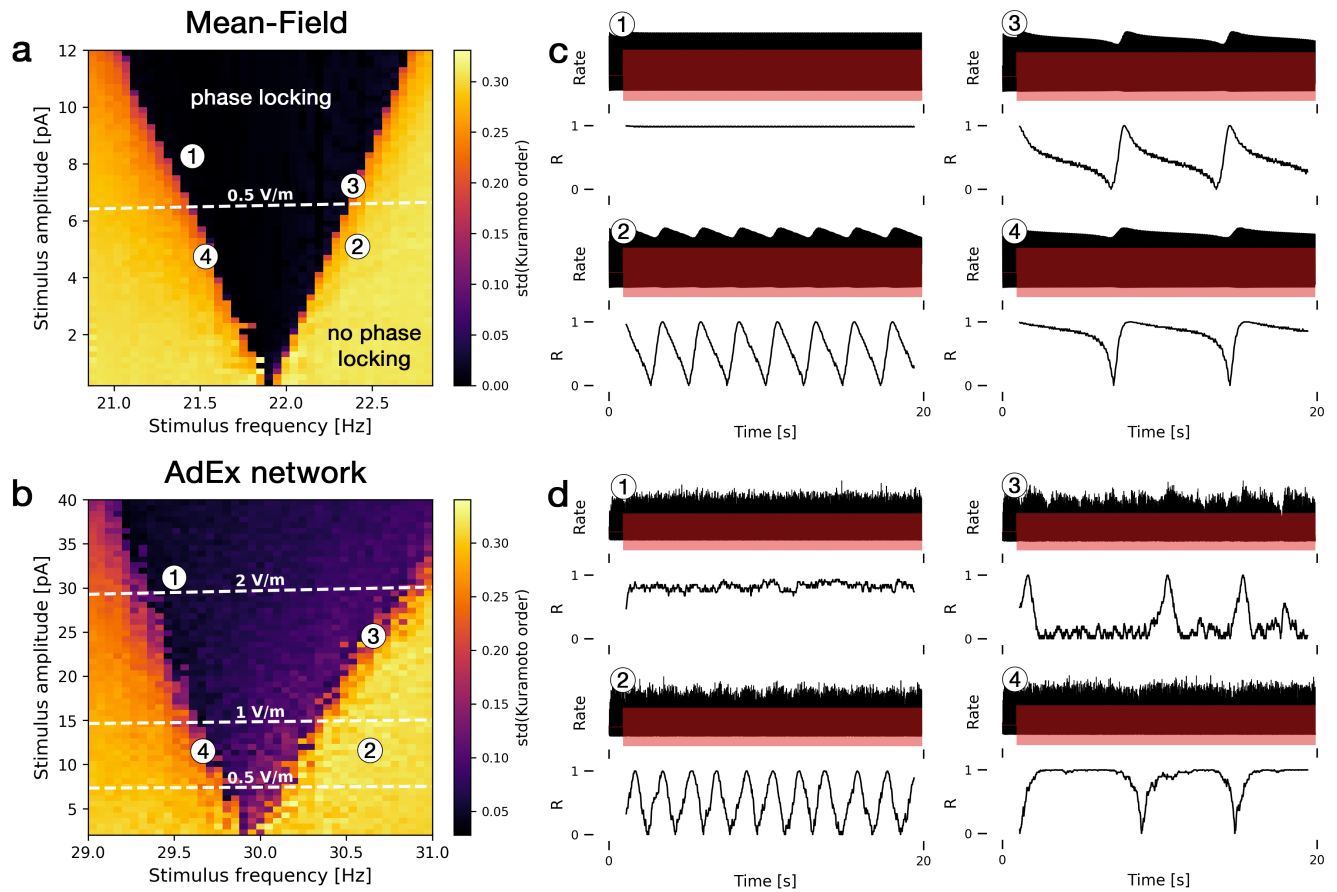


**Figure 6. Phase locking of ongoing oscillations via weak oscillatory inputs.** The left panels show heatmaps of (a) the mean-field model and (b) the AdEx network for different stimulus frequencies and amplitudes. The color indicates the level of phase locking, represented by dark areas for effective phase locking and bright yellow areas for no phase locking. Phase locking is measured by the standard deviation of the Kuramoto order parameter which is a measure for phase synchrony. White dashed lines indicate the strength of an equivalent external electric field in V/m that would correspond to the oscillating input current. (c) Time series of four points indicated in (a) with the excitatory population's rate in black and the external input in red (upper panel). In the lower panel, the Kuramoto order parameter  $R$  is shown which measures the synchrony between the population rate and the external input. Constant  $R$  represents effective phase locking (phase difference between rate and input is constant), fluctuating  $R$  indicates dephasing of both signals, hence no phase locking. (d) Corresponding time series of points in (b). Both models are parameterized to be in point A2 inside the fast oscillatory region  $LC_{EI}$ . All parameters are given in Table 1.

1). The mean-field model provides an accurate and computationally efficient approximation of the mean activity and mean membrane potentials of the AdEx network if all neurons are equal, the number of neurons is large, and the connectivity is sparse and random. The biophysical parameters of the AdEx network model are preserved in the mean-field description, enabling us to model realistic electric currents and equivalent extracellular field strengths<sup>31</sup> in various electrical stimulation scenarios.

Bifurcation diagrams (Figs. 2) provide a map of the possible states as a function of the external inputs to both, excitatory and inhibitory, populations. A comparison of the diagrams of the mean-field model to the corresponding AdEx network model reveals a high degree of similarity of the state spaces. Each attractor of the AdEx network is represented in the mean-field model in a one-to-one fashion which allows for accurate predictions about the state of the network using the low-dimensional mean-field model.

Without a somatic adaptation feedback mechanism, the population rate can occupy four distinct states: a *down-state* with very weak activity, an *up-state* with constant high activity representing an asynchronous firing of the neurons, a *bistable* regime where down-state and up-state coexist and an oscillatory state where the activity alternates between the excitatory and the inhibitory population at a low gamma frequency.

The AdEx neuron model allows for incorporation of a slow potassium-mediated adaptation current, typically found in cortical pyramidal neurons<sup>35</sup>. Due to somatic adaptation, in the bistable region the up-state loses its stability<sup>32,33</sup> and transforms into a second oscillatory regime caused by the slow feedback mechanism of the adaptation currents (Fig. 3). In this state, the population activity oscillates at delta frequencies. This oscillatory region coexists with the fast excitatory-inhibitory oscillation.

Using the bifurcation diagrams (Fig. 2), we mapped out several points of interest that represent different network states. The type of reaction to external stimulation depends on the current state of the system, as seen in the population time series during stimulation in Fig. 4. Close to edges of attractors, direct currents can cause bifurcations and trigger a sudden change of the dynamics, such as transitions from a low activity *down-state* to a state with oscillatory activity. Switching due to external fields has been observed *in vitro*<sup>3</sup> at similar field strengths of 6 V/m as we observed in the model.

It is worth mentioning that other parameters, such as coupling strengths and adaptation parameters, can cause bifurcations as well. Overall, the specific shape of the dynamical landscape depends on numerous parameters. However, parameter explorations using the mean-field model indicated that the overall structure of the bifurcation diagrams presented in this paper was fairly robust to changes of the coupling strengths (see Supplementary Fig. 12) and therefore representative for this E-I system.

Inside oscillatory regions, alternating input causes phase locking and frequency entrainment. To study how frequency entrainment depends on the frequency and amplitude of the stimulus, we analysed frequency spectrograms of the population activity when subject to external oscillating stimuli with increasing frequencies (Fig. 5). The necessary field amplitudes for this effect are on the order of endogenously generated fields in the *in vivo* brain<sup>10,11</sup> and in accordance with observations in *in vitro* experiments with field strengths of 3 – 6 V/m<sup>3,36</sup>. We found that the range of frequency entrainment around the natural frequency of the endogenous oscillation widens as the stimulus amplitude increases, which was observed in similar computational stimulation studies<sup>15,37</sup>. We also observed frequency entrainment with a stimulus of a frequency close to the higher harmonics of the endogenous oscillation. This effect could be valuable for experimental conditions where it is impractical to use stimulation frequencies close to the endogenous frequency of ongoing oscillations in the studied neural system.

If the stimulus frequency is close to the endogenous frequency (frequency matching), an oscillatory stimulus can force the ongoing oscillation to synchronize its phase with the stimulus, called phase entrainment or phase locking. Very weak input currents are able to phase lock ongoing oscillations, which correspond to external electric field strengths with amplitudes in the order of 1 V/m (Fig. 6). Our predicted field strengths are comparable to fields generated by stimulation techniques such as transcranial alternating current stimulation (tACS)<sup>38</sup> which were used to phase entrainment of brain oscillations<sup>13,39,40</sup> and are weaker than endogenously generated fields.

We found all observed input-dependent effects in the AdEx network to be well-represented by the mean-field model, which highlights its accuracy also in the non-stationary case. However, partly due to the difference of parameters that define the states in the bifurcation diagram, the AdEx network consistently requires larger input amplitudes in order to cause the same effect size as in the mean-field model (Figs. 5 and 6).

This is related to the fact that in the bifurcation diagrams Fig. 2, the shape of the oscillatory region as well as the amplitudes and frequencies of the oscillations differ (see Supplementary Fig. 11). We suspect that the oscillatory states are where the steady-state approximations that are used to construct the mean-field model break down due to the fast temporal dynamics in this state. Hence, both models have differences in frequencies and amplitudes within the oscillatory regions. This also affects at which parameter values the described bifurcations take place, resulting in a narrower limit cycle region in the mean-field approximation.

Overall, our observations confirm that a sophisticated mean-field model of a neural mass is appropriate for studying the macroscopic dynamics of large populations of spiking neurons consisting of excitatory and inhibitory units. To our knowledge, such a remarkable equivalence of the dynamical states between a mean-field neural mass model and its ground-truth spiking network model has not been demonstrated before. Our analysis shows that mean-field models are useful for quickly exploring

the parameter space in order to predict states and parameters of the neural network. Since the dynamical landscapes of both models are very similar, we believe that it should be possible to reproduce a variety of stationary and time-dependent properties of large-scale network simulations using low-dimensional population models. This may help to mechanistically describe the rich and plentiful observations in real neural systems when subject to stimulation with electric currents or electric fields, such as switching between bistable *up* and *down-state* states or phase and frequency entrainment of the population activity.

Bifurcations, as studied in dynamical systems theory, offer a plausible mechanism of how networks of neurons as well as the brain as a whole<sup>41,42</sup> can change its mode of operation. Understanding the state space of real neural systems could be beneficial for developing electrical stimulation techniques and protocols, represented as trajectories in the dynamical landscape, which could be used to reach desirable states or specifically inhibit pathological dynamics.

Because of the variety of possible macroscopic network states that arise from the basic E-I architecture, it is critical to consider the state of the system in order to understand its response to external stimuli. Therefore, we expect that in order to account for the numerous seemingly inconclusive experimental results from noninvasive brain stimulation studies<sup>12</sup>, additional to the stimulus parameters<sup>5</sup>, the response of a system to external stimuli has to be understood in context of the dynamical state of the unperturbed system<sup>3,14,15</sup>.

## Methods

### Neural population setting

In order to derive the mean-field description of an AdEx network, we consider a very large number of  $N \rightarrow \infty$  neurons for each of the two populations  $E$  and  $I$ . We assume (1) random connectivity (within and between populations), (2) sparse connectivity<sup>43,44</sup>, but each neuron having a large number of inputs<sup>45</sup>  $K$  with  $1 \ll K \ll N$ , (3) and that each neuron's input can be approximated by a Poisson spike train<sup>46,47</sup> where each incoming spike causes a small ( $c \ll 1$ ) and quasi-continuous change of the postsynaptic potential (PSP)<sup>48</sup> (*diffusion approximation*).

### The spiking neuron model

The adaptive exponential (AdEx) integrate-and-fire neuron model forms the basis for the derivation of the mean-field equations as well as the spiking network simulations. Each population  $\alpha \in \{E, I\}$  has  $N_\alpha$  neurons which are indexed with  $i \in [0, N_\alpha]$ . The membrane voltage of neuron  $i$  in population  $\alpha$  is governed by

$$C \frac{dV_i}{dt} = I_{\text{ion}}(V_i) + I_i(t) + I_{i,\text{ext}}(t), \quad (1)$$

$$I_{\text{ion}}(V) = g_L(V - E_L) + g_L \Delta_T \exp\left(\frac{V - V_T}{\Delta_T}\right) - I_A(t). \quad (2)$$

The first term of  $I_{\text{ion}}$  describes the voltage-dependent leak current, the second term the nonlinear spike initiation mechanism, and the last term the somatic adaptation current.  $I_{i,\text{ext}}(t) = \mu^{\text{ext}}(t) + \sigma^{\text{ext}} \xi_i(t)$  is a noisy external input. It consists of a mean current  $\mu^{\text{ext}}(t)$  which is equal across all neurons of a population and independent Gaussian fluctuations  $\xi_i(t)$  with standard deviation  $\sigma^{\text{ext}}$  ( $\sigma^{\text{ext}}$  is equal for all neurons of a population). For a neuron in population  $\alpha$ , synaptic activity induces a postsynaptic current  $I_i$  which is a sum of excitatory and inhibitory contributions:

$$I_i(t) = C(J_{\alpha E} s_{i,\alpha E}(t) + J_{\alpha I} s_{i,\alpha I}(t)), \quad (3)$$

with  $C$  being the membrane capacitance and  $J_{\alpha\beta}$  the coupling strength from population  $\beta$  to  $\alpha$ , representing the maximum current when all synapses are active. Its dynamics is given by

$$\frac{ds_{i,\alpha\beta}}{dt} = -\frac{s_{i,\alpha\beta}}{\tau_s} + \frac{c_{\alpha\beta}}{J_{\alpha\beta}} (1 - s_{i,\alpha\beta}) \sum_j G_{ij} \sum_k \delta(t - t_j^k - d_{\alpha\beta}). \quad (4)$$

$s_{i,\alpha\beta}(t)$  represents the fraction of active synapses from population  $\beta$  to  $\alpha$  and is bound between 0 and 1.  $G_{ij}$  is a (random) binary connectivity matrix with constant rowsum  $K_\alpha$  and connects neurons  $j$  of population  $\beta$  to neurons  $i$  of population  $\alpha$ . With the constraint of a constant in-degree  $K_\alpha$  of each unit, all neurons of population  $\beta$  project to neurons of population  $\alpha$  with a probability of  $p_{\alpha\beta} = K_\alpha/N_\beta$  and  $\alpha, \beta \in \{E, I\}$ .  $G_{ij}$  is generated independently for every simulation. The first term in Eq. 4 is an exponential decay of the synaptic activity, whereas the second term integrates all incoming spikes as long as  $s_{i,\alpha\beta} < 1$  (i.e. some synapses are still available). The first sum is the sum over all afferent neurons  $j$ , and the second sum is the sum over all incoming spikes  $k$  from neuron  $j$  emitted at time  $t^k$  after a delay  $d_{\alpha\beta}$ . If  $s_{i,\alpha\beta} = 0$ , the amplitude of the postsynaptic current is exactly  $C \cdot c_{\alpha\beta}$  which we set to values from physiological *in-vitro* measurements<sup>49</sup> (see Table 1).

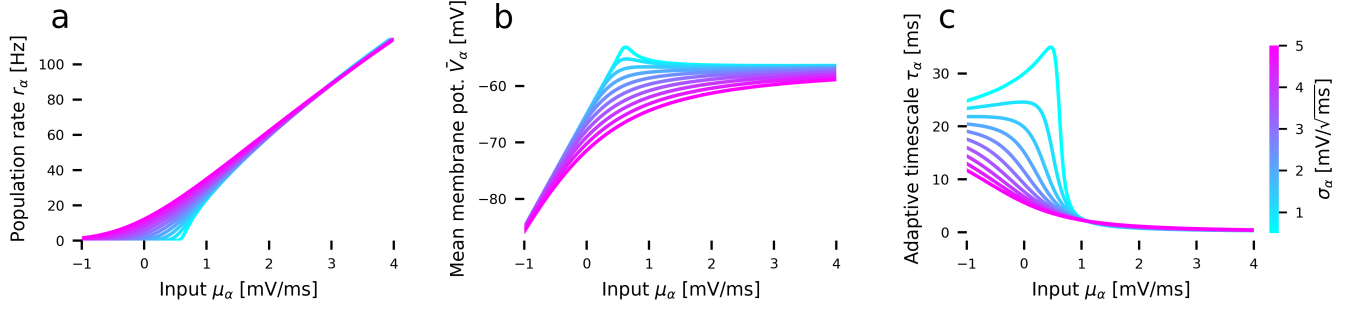


**Figure 7. Precomputed quantities of the linear-nonlinear cascade model.** (a) Nonlinear transfer function  $\Phi$  for the mean population rate (Eq. 15 in the main manuscript) (b) Transfer function for the mean membrane voltage (Eq. 10 in the main manuscript) (c) Time constant  $\tau_\alpha$  of the linear filter that approximates the linear rate response function of an AdEx neuron (Eq. 7 in the main manuscript). Color scale represents the level of the input current variance  $\sigma_\alpha$  across the population. All neuronal parameters are given in Table 1 in the main manuscript.

For neurons  $i$  of the excitatory population, the adaptation current  $I_{A,i}(t)$  is given by

$$\tau_A \frac{dI_{A,i}}{dt} = a(V_i - E_A) - I_{A,i}, \quad (5)$$

$a$  representing the subthreshold adaptation and  $b$  the spike-dependent adaptation parameters. The inhibitory population doesn't have an adaptation mechanism, which is equivalent to setting these parameters to 0. When the membrane voltage crosses the spiking threshold,  $V_i \geq V_s$ , the voltage is reset,  $V_i = V_r$ , clamped for a refractory time  $T_{\text{ref}}$ , and the spike-triggered adaptation increment is added to the adaptation current,  $I_{A,i} = I_{A,i} + b$ . All parameters are given in Table 1.

Finally, we define the mean firing rate of neurons in population  $\alpha$  as

$$r_\alpha(t) = \frac{1}{N_\alpha} \frac{1}{dt} \sum_{i=0}^{N_\alpha} \int_i^{i+dt} \delta(t' - t_i^k) dt, \quad (6)$$

which measures the number of spikes in a time window  $dt$ , set to the integration step size in our numerical simulations.

### The mean-field neural mass model

For a sparsely connected random network of AdEx neurons as defined by Eqs. 1-5, the distribution of membrane potentials  $p(V)$  and the mean population firing rate  $r$  can be calculated using the Fokker-Planck equation in the thermodynamic limit  $N \rightarrow \infty$ <sup>16,50</sup>. Determining the distribution involves solving a partial differential equation, which is computationally demanding. A low-dimensional linear-nonlinear cascade model<sup>27,51</sup> can be used to capture the steady-state and transient dynamics of a population in form of a set of simple ODEs. Briefly, for a given mean membrane current  $\mu_\alpha$  with standard deviation  $\sigma_\alpha$ , the mean of the membrane potentials  $\bar{V}_\alpha$  as well as the population firing rate  $r_\alpha$  in the steady-state can be calculated from the Fokker-Planck equation<sup>52</sup> and captured by a set of simple nonlinear transfer functions  $\Phi(\mu_\alpha, \sigma_\alpha)$  (shown in Figs. 7 a and b).

The reproduction accuracy of the linear-nonlinear cascade model in the form a simple ODE system for a single population has been systematically reviewed in Ref.<sup>26</sup> and has been shown to reproduce the dynamics of an AdEx network in a range of different input regimes quite successfully, while offering significant increase in computational efficiency.

### Rate equations

The derivation of the equations that govern the mean  $\mu_\alpha$  and variance  $\sigma_\alpha^2$  of the membrane currents, the mean adaptation current  $\bar{I}_A$ , and the mean  $\bar{s}_{\alpha\beta}$  and variance  $\sigma_{s,\alpha\beta}^2$  of the synaptic activity are presented further below. The full set of equations of the mean-field model reads:

$$\tau_\alpha \frac{d\mu_\alpha}{dt} = \mu_\alpha^{\text{syn}}(t) + \mu_\alpha^{\text{ext}} - \mu_\alpha(t), \quad (7)$$

$$\mu_\alpha^{\text{syn}}(t) = J_{\alpha E} \bar{s}_{\alpha E}(t) + J_{\alpha I} \bar{s}_{\alpha I}(t), \quad (8)$$

$$\sigma_\alpha^2(t) = \sum_{\beta \in \{E, I\}} \frac{2J_{\alpha\beta}^2 \sigma_{s,\alpha\beta}^2(t) \tau_{s,\beta} \tau_m}{(1 + r_{\alpha\beta}(t)) \tau_m + \tau_{s,\beta}} + \sigma_{\text{ext},\alpha}^2, \quad (9)$$

$$\frac{d\bar{I}_A}{dt} = \tau_A^{-1} (a(\bar{V}_E(t) - E_A) - \bar{I}_A) + b \cdot r_E(t), \quad (10)$$

$$\frac{d\bar{s}_{\alpha\beta}}{dt} = -\tau_{s,\beta}^{-1} \bar{s}_{\alpha\beta}(t) + (1 - \bar{s}_{\alpha\beta}(t)) \cdot r_{\alpha\beta}(t), \quad (11)$$

$$\frac{d\sigma_{s,\alpha\beta}^2}{dt} = (1 - \bar{s}_{\alpha\beta}(t))^2 \cdot \rho_{\alpha\beta}(t) + \tau_{s,\beta}^{-2} (\rho_{\alpha\beta}(t) - 2\tau_{s,\beta}(\rho_{\alpha\beta}(t) + 1)) \cdot \sigma_{s,\alpha\beta}^2(t), \quad (12)$$

for  $\alpha, \beta \in \{E, I\}$ . All parameters are listed in Table 1. The mean  $r_{\alpha\beta}$  and the variance  $\rho_{\alpha\beta}$  of the effective input rate from population  $\beta$  to  $\alpha$  for a spike transmission delay  $d_{\alpha\beta}$  are given by

$$r_{\alpha\beta}(t) = \frac{c_{\alpha\beta}}{J_{\alpha\beta}} K_\beta \cdot r_\beta(t - d_\alpha), \quad (13)$$

$$\rho_{\alpha\beta}(t) = \frac{c_{\alpha\beta}}{J_{\alpha\beta}} \cdot r_{\alpha\beta}(t). \quad (14)$$

$r_\alpha$  is the instantaneous population spike rate,  $c_{\alpha\beta}$  describes the amplitude of the post-synaptic current caused by a single spike (at rest,  $s_{\alpha\beta} = 0$ ) and  $J_{\alpha\beta}$  the maximum membrane current generated when all synapses are active (at  $s_{\alpha\beta} = 1$ ).

To account for the transient dynamics of the population to a change of the membrane currents,  $\mu_\alpha$  can be integrated by convolving the input with a linear response function. This function is well-approximated by a decaying exponential<sup>26,27,51</sup> with a time constant  $\tau_\alpha$  (shown in Fig. 7 c). Thus, the convolution can simply be expressed as an ODE (Eq. 7). Here,  $\mu_\alpha^{\text{syn}}(t)$ , as defined by Eq. 8, represents the mean current caused by synaptic activity and  $\mu_\alpha^{\text{ext}}$  the currents caused by external stimulation. The instantaneous population spike rate  $r_\alpha$  is determined using the precomputed nonlinear transfer function

$$r_\alpha = \Phi(\mu_\alpha, \sigma_\alpha). \quad (15)$$

The transfer function  $\Phi$  is shown in Fig. 7 a. It translates the mean  $\mu_\alpha$  as well as the standard deviation  $\sigma_\alpha$  (Eq. 9) of the membrane currents into a population firing rate. Using an efficient numerical scheme<sup>27,52</sup>, this function was previously computed<sup>26</sup> from the steady-state firing rates of a population of AdEx neurons given a particular input mean and standard deviation. The transfer function depends on the parameters of the single AdEx neuron. Equation 10 governs the evolution of the mean adaptation current of the excitatory population. Equations 11 and 12 describe the mean and standard deviation of the fraction of active synapses caused by incoming spikes from the population  $\beta$  to population  $\alpha$ .

### Synaptic model

Following Ref.<sup>53</sup>, we derive ODE expressions for the population mean  $\bar{s}_{\alpha\beta}$  and variance  $\sigma_{s,\alpha\beta}^2$  of the synaptic activity. We rewrite the synaptic activity given by Eq. 4 of a neuron  $i$  from population  $\alpha$  caused by inputs from population  $\beta$  with  $\alpha, \beta \in \{E, I\}$  in terms of a continuous input rate  $r_\beta$  (*diffusion approximation*) such that

$$\tau_{s,\beta} \frac{ds_{i,\alpha\beta}}{dt} = -s_i + \frac{c_{\alpha\beta}}{J_{\alpha\beta}} (1 - s_i) \left( K_\alpha r_\beta(t - d_\alpha) + \sqrt{K_\alpha r_\beta(t - d_\alpha)} \xi_i(t) \right), \quad (16)$$

with  $K_\alpha = \sum_{j \in \alpha} G_{ij}$  being the constant in-degree of each neuron,  $r_\beta(t - d_\alpha)$  the incoming delayed mean spike rate from all afferents of population  $\beta$ , and  $\xi_i(t)$  is standardized Gaussian white noise. The current  $I_i(t)$  of a neuron in population  $\alpha$  due to synaptic activity is given by

$$I_i(t) = \sum_{\beta \in \{E, I\}} C J_{\alpha\beta} s_{i,\alpha\beta}(t). \quad (17)$$

We split the mean from the variance of Eq. 16 by first taking the mean over neurons of Eq. 16. The mean synaptic activity  $\bar{s}_{\alpha\beta} := \langle s_{i,\alpha\beta} \rangle_i$  of population  $\alpha$  caused by input from population  $\beta$  is then given by Eq. 11. We get the differential equation of the variance  $\sigma_{s,\alpha\beta}^2$  of  $s_{i,\alpha\beta}$  in Eq. 12 by applying Ito's product rule on  $d(s_{i,\alpha\beta}^2)$  and taking its time derivative.



### Input currents

Additional to the mean currents (Eq. 7) in the population, we also keep track of its variance. Figure 7 shows the population firing rate and mean membrane potential for different levels of variance of the membrane currents. Especially the adaptive time-constant, which affects the temporal dynamics of the population's response, strongly depends on the variance of the input. Without loss of generality, we derive the variance of the membrane currents caused by a single afferent population  $\alpha$  and later add up the contributions of two coupled populations (excitatory and inhibitory). Assuming that every neuron receives a large number of uncorrelated inputs (*white noise approximation*), we write the synaptic current  $I_{i,\alpha}(t)$  in terms of contributions to the population mean and the variance<sup>16,54-57</sup>:

$$I_{i,\alpha}(t) = C(\mu_\alpha(t) + \sigma_\alpha(t)\xi_i(t)). \quad (18)$$

In order to obtain the contribution of synaptic input to the mean and the variance of membrane currents, we (1) neglect the exponential term of  $I_{\text{ion}}$  in Eq. 2 and (2) assume that the membrane voltages are mostly subthreshold such that we can neglect the nonlinear reset condition. Numerical simulations have proven that these assumptions are justifiable in the parameter ranges that we are concerned with<sup>53</sup>. We apply these simplifications only in this step of the derivation. The exponential term, the neuronal parameters within it, and the reset condition still affect the precomputed functions (shown in Fig. 7) and thus the overall population dynamics.

We substitute both approximations Eq. 17 and Eq. 18 separately into the membrane voltage Eq. 1 and apply the expectation operator on both sides, which leads to two equations describing the evolution of the mean membrane potential. If we require that both approximations should yield the same mean potential  $\langle V_{i,\alpha} \rangle$ , we can easily see that  $\mu_\alpha^{\text{syn}}(t) = J_{\alpha\alpha} \langle s_{i,\alpha\alpha}(t) \rangle$ . Using Ito's product rule<sup>58</sup> on  $dV^2$  and requiring that both approximations should also result in the same evolution of the second moment  $\langle V_\alpha^2 \rangle$ , we get

$$\sigma_\alpha^2(t) = 2J_{\alpha\alpha} (\langle V_{i,\alpha} s_{i,\alpha\alpha} \rangle - \langle V_{i,\alpha} \rangle \langle s_{i,\alpha\alpha} \rangle). \quad (19)$$

Taking the time derivative of Eq. 19 and substituting the time derivative of  $\langle V_\alpha s_{\alpha\alpha} \rangle$  by applying Ito's product rule on  $d(V_\alpha s_{\alpha\alpha})$  we obtain

$$\frac{d\sigma_\alpha^2}{dt} = 2J_{\alpha\alpha}^2 \sigma_{s,\alpha\alpha}^2(t) - \left( \frac{c\tau_\alpha K r_{\alpha\alpha}(t) + 1}{\tau_{s,\alpha}} + \frac{1}{\tau_m} \right) \sigma_{s,\alpha\alpha}^2(t) \quad (20)$$

Here,  $\sigma_{s,\alpha\alpha}^2 := \langle s_{i,\alpha\alpha}^2 \rangle - \langle s_{i,\alpha\alpha} \rangle^2$ . The timescale of Eq. 20 is much smaller than  $\tau_\alpha$  of Eq. 7. We can therefore approximate  $\sigma_\alpha^2(t)$  well with its steady-state value:

$$\sigma_\alpha^2(t) = \frac{2J_{\alpha\alpha}^2 \tau_m \tau_\alpha \sigma_{s,\alpha\alpha}^2(t)}{(c\tau_\alpha K r_{\alpha\alpha}(t) + 1) \tau_m + \tau_{s,\alpha}}, \quad (21)$$

$\tau_m = C/g_L$  being the membrane time constant. Adding up the variances in Eq. 21 of both E and I subpopulations and the variance of the external input  $\sigma_{\text{ext},\alpha}^2$ , the total variance of the input currents is then given by Eq. 9. The two moments of the membrane currents,  $\mu_\alpha$  and  $\sigma_\alpha$ , fully determine the instantaneous firing rate  $r_\alpha = \langle r_i \rangle_i$  (Eq. 15), the mean membrane potential  $\bar{V}_\alpha := \langle V_i \rangle_i$ , and the adaptive timescale  $\tau_\alpha$  (Fig. 7).

### Adaptation mechanism

The large difference of timescales of the slow adaptation mechanism mediated through  $\text{K}^+$  channel dynamics compared to the faster membrane voltage dynamics<sup>59,60</sup> and synaptic dynamics allows for a separation of timescales<sup>61</sup> (*adiabatic approximation*). Therefore, each neuron's adaptation current can be approximated by its population average  $\bar{I}_A$ , which evolves according to Eq. 10, where  $a$  is the sub-threshold adaptation and  $b$  is the spike-triggered adaptation parameter.  $\bar{V}_\alpha(t) = \bar{V}_\alpha(\mu_\alpha, \sigma_\alpha)$  is the mean of the membrane potentials of the population and was precomputed and is read from a table (Fig. 7 b) at every timestep. In the case of  $a, b > 0$ , when adaptation is active, we subtract the current  $\bar{I}_A$  caused by the adaptation mechanism from the current  $C \cdot \mu_\alpha$  caused by the synapses in order to obtain the net input current. The resulting firing rate of the excitatory population is then determined by evaluating  $r_E = \Phi(\mu_E - \bar{I}_A/C, \sigma_E)$ . For fast-spiking inhibitory neurons, adaptation was neglected ( $a = b = 0$ ) since the adaptation mechanism was found to be much weaker than in the case of pyramidal cells<sup>62</sup>.

### Obtaining bifurcation diagrams and determining bistability

Each point in the bifurcation diagrams in Figs. 2 and 3 were simulated for each pair of external inputs  $\mu_E^{\text{ext}}$  and  $\mu_I^{\text{ext}}$  and the resulting time series of the excitatory population rate of the mean-field model and the AdEx network were analysed and the dynamical state was classified.

To classify a point in the state space as *bistable* or not, in both models, the mean-field model as well as the AdEx network, we apply a negative and a subsequent positive stimulus to the excitatory population and measure the difference in activity after

both stimuli are turned off again. In the AdEx network, a simple step input can cause over- and under-shoot as a reaction, which is a problem when assessing the stability of a basin of attraction around a fixed point. To overcome this problem, we constructed a slowly-decaying stimulus (in contrast to previous work<sup>63</sup>, where bistability was identified using a step current). An inverted example of this stimulus is shown in Figs. 4 e and f. Using this stimulus, we first made sure that the population rate is in the *down-state*, the initial state, with an initial negative external input current that slowly decays back to zero. We then kicked the activity into the *up-state* (the target state) with a positive input and then let the current slowly decay to zero again. A slowly-decaying stimulus (in contrast to a step stimulus) ensures that transient effects such as over- and undershooting are minimized that would otherwise disturb the target state. As a result, the stability of the target state can be observed. We determined whether the *up-state* is stable or the activity has decayed back into the *down-state* by comparing the 1 s mean of the population rates after both stimuli have decayed. We classified a state as bistable if the rate difference after both kicks and subsequent relaxation phases was greater than 10Hz. This threshold value was chosen to be smaller than every observed difference between the *up-* and the *down-state*. We confirmed the validity of this method for the mean-field model by using a continuation method to determine the stability of the fixed-point states, which provided the same bifurcation diagrams,

### Determining frequency spectra of the population activity

In the bifurcation diagrams in Figs. 2 and 3, regions were classified as oscillating if the time series showed oscillations during the last 1 s after the first (negative) stimulus pushed the system into the *down-state*. The power spectrum of this oscillation was computed using the implementation of Welch's method<sup>64</sup> `scipy.signal.welch` in the python package SciPy (1.2.1)<sup>65</sup>. A rolling Hanning window of length 0.5s was used to compute the spectrum. If the dominant frequency was above 0.1 Hz and its power density was above 1 Hz we classified the state as oscillating. Visual observation of the time series confirmed that these thresholds classified the oscillating regions well. In cases where the transient of 1 s was too short such that the activity state of the population jumped from the *down-state* to the *up-state* within this period, misclassifications of these points as oscillatory states caused artifacts at the right-hand border of the *bistable* region to the *up-state*.

In Fig. 5, we determined *frequency entrainment* by observing changes of the frequency spectrum of the population activity  $r_E$ . Each run was simulated for 6s. We waited for 1s for transient effects to vanish before turning on the oscillating stimulus and measured the power spectrum of the remaining 5s. A rolling Hanning window of length 1 s was used. For better visibility, the power was normalized between 0 and 1 on a logarithmic scale and plotted with a linear colormap.

### Measuring phase locking using the Kuramoto order parameter

In Fig. 6 we quantified the degree of phase locking of an oscillatory input current with the E-I system's ongoing oscillation. We calculated the Kuramoto order parameter<sup>66</sup> to measure phase synchrony. The Kuramoto order parameter  $R$  is given by:

$$R(t) = \frac{1}{N_{\text{osc}}} \left| \sum_{j=1}^{N_{\text{osc}}} e^{i\Phi_j(t)} \right|. \quad (22)$$

In our case, the number of oscillators  $N_{\text{osc}} = 2$  and  $\Phi_j \in [0, 2\pi)$  is the instantaneous phase of the stimulus ( $j = 1$ ) and the population activity  $r_E$  ( $j = 2$ ). We define the phase  $\Phi_{hi_j}$  as

$$\Phi_j(t) = 2\pi \frac{t - t_n}{t_n - t_{n-1}}, \quad (23)$$

where  $t_n$  is the time of the last maximum (from time  $t$ ) of the time series and  $t_{n-1}$  the penultimate one. To robustly detect the oscillation maxima of the noisy AdEx network population rate, the time series was first smoothed using the Gaussian filter `scipy.ndimage.filters.gaussian_filter` implemented in SciPy. The Gaussian kernel had a standard deviation of 5. Then, the maxima were detected using the peak finding algorithm `scipy.signal.find_peaks_cwt` with a peak-width between 0.1 and 0.2.

For  $R = 1$ , perfect (zero-lag) phase synchronization is reached; if  $R \approx 0$ , the oscillations are maximally desynchronized. To measure *phase locking* in Figs. 6 a and c, we calculated the standard deviation of  $R(t)$  in time after transient effects vanish for  $t > 1.5$ s. A low standard deviation indicates that the phase difference between the input and the ongoing oscillation stays constant.

### Calculating equivalent electric field strengths

Our results can be used to estimate the necessary amplitude of an external electric field to reproduce the effects of electrical input currents which we have investigated here. An external field at the location of a neural population might be produced by endogenous electric fields due to the activity of a neural population or external stimulation techniques such as transcranial electrical stimulation (tES) with direct (tDCS) or alternating (tACS) currents. The lack of a spatial extension of point neuron models such as the AdEx neuron makes it impossible to directly couple an external electric field that could affect the internal

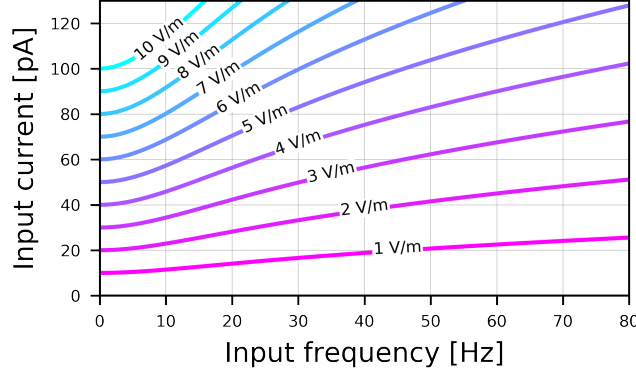


**Figure 8. Conversion between electric field amplitudes and equivalent input currents.** Curves show frequency-dependent amplitudes for an input current in pA to an exponential integrate-and-fire neuron with parameters as defined in Table 1 (in the main manuscript) when the electric field amplitude acting on an equivalent ball-and-stick neuron is held constant. Electric field amplitudes in V/m are annotated for each curve.

membrane voltages. Following Ref.<sup>31</sup> we obtain an equivalent electrical input  $C \cdot \mu_E^{\text{ext}}(t)$  to a point neuron by matching it to reproduce the effects of an oscillating extracellular electric field on a spatially extended ball-and-stick (BS) model neuron of a given morphology. The point neuron model for which we calculated the equivalent current amplitudes is the exponential integrate-and-fire (EIF) neuron, which is the same as the AdEx neuron without somatic adaptation ( $a = b = 0$ ). In the case with adaptation, the translation from current to field works for high frequency inputs only and the approximation breaks down for slowly oscillating inputs. We have limited our estimations to the case without adaptation.

The amplitude of the equivalent input current that causes the same subthreshold depolarization of an (linearized) EIF neuron as the somatic depolarization caused by the effects of an oscillatory electric field on the BS neuron's dendrite is then calculated using

$$I_{\text{ext}} = A \left| \frac{U_{\text{BS}}(f)}{z_{\text{EIF}}(f)} \right| \quad (24)$$

$A$  is the amplitude of the electric field in V/m,  $U_{\text{BS}}(f)$  is the frequency-dependent polarization transfer function of the BS neuron and  $z_{\text{EIF}}(f)$  is the impedance of the EIF neuron which are given by

$$U_{\text{BS}}(f) = g_a(2e^{-z l_d} - \gamma) / \delta \quad (25)$$

$$z_{\text{EIF}}(f) = \frac{1}{g_L(1 - e^{\frac{V_r - V_r}{\Delta T}}) + 2\pi i C \cdot f} \quad (26)$$

with the following substitutions:

$$w = 2\pi f, \quad g_m = (\pi d_d) / \rho_m, \quad g_a = (\pi (d_d/2)^2) / \rho_a \quad (27)$$

$$c_m = C_m d_d \pi, \quad g_s = (\pi d_s^2) / \rho_s, \quad c_s = C_m \pi d_s^2 \quad (28)$$

$$\alpha = \sqrt{\frac{g_m + \sqrt{g_m^2 + w^2 c_m^2}}{2g_a}}, \quad \beta = \sqrt{\frac{-g_m + \sqrt{g_m^2 + w^2 c_m^2}}{2g_a}} \quad (29)$$

$$z = \alpha + i\beta, \quad \gamma = 1 + \exp(-2l_d z), \quad \delta = \gamma(c_s w i + g_s) + z g_a (2 - \gamma) \quad (30)$$

The BS neuron we used to estimate electric field strengths has the following parameters: The soma has a diameter of  $d_s = 10 \mu\text{m}$ , a specific membrane capacitance of  $C_m = 10 \text{mF}/\text{m}^2$  and a membrane resistivity of  $\rho_s = 2.8 \Omega\text{m}^2$ . The dendritic cable has a length of  $l_d = 1200 \mu\text{m}$ , a diameter of  $d_d = 2 \mu\text{m}$ , a membrane resistivity of  $\rho_m = 2.8 \Omega\text{m}^2$  and an axial resistivity of  $\rho_a = 1.5 \Omega\text{m}$ .

Using these parameters, an step input using an electric field with an amplitude of 1 V/m changes the somatic membrane potential by about 0.1 mV from its resting potential of  $-65 \text{mV}$ . The curves in Fig. 8 translate an electric field of a given amplitude and frequency into a corresponding input current and vice versa. An increase of the mean membrane current by 0.1 nA corresponds to an increase of the static electric field strength by 11 V/m. This

## Numerical simulations

The mean-field equations were integrated using the forward Euler method. In Figs. 2 each time series for a set of external inputs  $\mu_E^{\text{ext}}$  and  $\mu_I^{\text{ext}}$  in the bifurcation diagrams was obtained after  $t = 5$  s simulation with an integration timestep of  $dt = 0.05$  ms. In Fig. 3 we simulated each point for  $t = 10$  s with  $dt = 0.01$  ms. For Figs. 5 we simulated for  $t = 30$  s with  $dt = 0.05$  ms.

The spiking network model was implemented using BRIAN2<sup>67</sup> (2.1.3.1) in Python. The equations were integrated using the implemented Heun’s integration method. An integration step size of 1 ms was used. For the bifurcation diagrams in Figs. 2, we used  $N = 2 \times 25000$  (i.e. 25000 per population), a total simulation time of  $t = 6$  s and in Fig. 3,  $N = 2 \times 10000$ ,  $t = 6$  s. The stimulation experiments in Fig. 4 used  $N = 2 \times 50000$ ,  $t = 3$  s. The spectra in Fig. 5 used  $N = 2 \times 10000$ ,  $t = 6$  s. Phase locking plots in Fig. 6 used  $N = 2 \times 10000$ ,  $t = 20$  s.

Benchmarking the AdEx network with  $N = 2 \times 50000$  on a single core took around  $10^4$  times longer to run than the corresponding mean-field simulation. This does not include the time required for initialization of the simulation, such as setting up all synapses, which can also requires a comparable amount of time. The computation time scales nearly linearly with the number of neurons.

## Tables

Parameter	Value	Description
$\sigma^{\text{ext}}$	$1.5 \text{ mV}/\sqrt{\text{ms}}$	Standard deviation of external input
$K_e$	800	Number of excitatory inputs per neuron
$K_i$	200	Number of inhibitory inputs per neuron
$c_{EE}, c_{IE}$	$0.3 \text{ mV/ms}$	Maximum AMPA PSC amplitude <sup>49</sup>
$c_{EI}, c_{II}$	$0.5 \text{ mV/ms}$	Maximum GABA PSC amplitude, <sup>49</sup>
$J_{EE}$	$2.4 \text{ mV/ms}$	Maximum synaptic current from E to E
$J_{IE}$	$2.6 \text{ mV/ms}$	Maximum synaptic current from E to I
$J_{EI}$	$-3.3 \text{ mV/ms}$	Maximum synaptic current from I to E
$J_{II}$	$-1.6 \text{ mV/ms}$	Maximum synaptic current from I to I
$\tau_{s,E}$	2 ms	Excitatory synaptic time constant
$\tau_{s,I}$	5 ms	Inhibitory synaptic time constant
$d_E$	4 ms	Synaptic delay to excitatory neurons
$d_I$	2 ms	Synaptic delay to inhibitory neurons
$C$	200 pF	Membrane capacitance
$g_L$	10 nS	Leak conductance
$\tau_m$	$C/g_L$	Membrane time constant
$E_L$	-65 mV	Leak reversal potential
$\Delta_T$	1.5 mV	Threshold slope factor
$V_T$	-50 mV	Threshold voltage
$V_s$	-40 mV	Spike voltage threshold
$V_r$	-70 mV	Reset voltage
$T_{\text{ref}}$	1.5 ms	Refractory time
$a$	15 nS	Subthreshold adaptation conductance
$b$	40 pA	Spike-triggered adaptation increment
$E_A$	-80 mV	Adaptation reversal potential
$\tau_A$	200 ms	Adaptation time constant

**Table 1.** Summary of the model parameters. Parameters apply for the Mean-Field model and the spiking AdEx network.

## Data and Code availability

The python code including the implementation of the models, the simulation pipeline, the stimulation experiments, as well as the data analysis and the ability to reproduce Figs. 2-6 can be found in our github repository under the URL [https://github.com/caglarcakan/stimulus\\_neural\\_populations](https://github.com/caglarcakan/stimulus_neural_populations). The code is released under the BSD 2 license.

All data can be reproduced using the code found in our github repository. The data that was used in this study are available from the corresponding author upon request.

Point	Mean-Field model		AdEx network		Dynamical state
	$C \cdot \mu_E^{\text{ext}}$	$C \cdot \mu_I^{\text{ext}}$	$C \cdot \mu_E^{\text{ext}}$	$C \cdot \mu_I^{\text{ext}}$	
A1	0.24	0.24	0.22	0.12	down
A2	0.26	0.1	0.32	0.3	LC <sub>EI</sub>
A3	0.41	0.34	0.4	0.24	bi
B3	0.8	0.36	0.76	0.24	LC <sub>aE</sub>
B4	0.76	0.4	0.68	0.24	down

**Table 2.** Values of the mean external inputs to the excitatory ( $\mu_E^{\text{ext}}$ ) and the inhibitory population ( $\mu_I^{\text{ext}}$ ) in units of nA for points of interest in the bifurcation diagrams Fig. 2.

## Acknowledgements

We would like to thank Dr. Josef Ladenbauer for his previous work on reduced population models, mathematical guidance, and many insightful discussions. We would like to thank Dr. Florian Aspart his work on the effects of extracellular electric fields, for helping to incorporate the results in this article, and for a helpful exchange of ideas. This work was supported by the Deutsche Forschungsgemeinschaft (DFG, German Research Foundation) with the project number 327654276 (SFB 1315) and the Research Training Group GRK1589/2.

## Author contributions

C.C. conducted the numerical simulations and wrote the manuscript, C.C. and K.O. analysed the results. All authors reviewed the manuscript.

## Competing interests

The authors declare no competing interests.



## References

1. Doron, G. & Brecht, M. What single-cell stimulation has told us about neural coding. *Philosophical Transactions of the Royal Society B: Biological Sciences* **370** (2015).
2. Lynch, E. P. & Houghton, C. J. Parameter estimation of neuron models using in-vitro and in-vivo electrophysiological data. *Frontiers in Neuroinformatics* **9**, 1–15 (2015).
3. Reato, D., Rahman, A., Bikson, M. & Parra, L. C. Low-Intensity Electrical Stimulation Affects Network Dynamics by Modulating Population Rate and Spike Timing. *Journal of Neuroscience* **30**, 15067–15079 (2010).
4. Reato, D., Rahman, A., Bikson, M. & Parra, L. C. Effects of weak transcranial alternating current stimulation on brain activity—a review of known mechanisms from animal studies. *Frontiers in Human Neuroscience* **7**, 1–8 (2013).
5. Thut, G. *et al.* Guiding transcranial brain stimulation by EEG/MEG to interact with ongoing brain activity and associated functions: A position paper. *Clinical Neurophysiology* **128**, 843–857 (2017).
6. Neuling, T., Rach, S., Wagner, S., Wolters, C. H. & Herrmann, C. S. Good vibrations: oscillatory phase shapes perception. *Neuroimage* **63**, 771–778 (2012).
7. Herrmann, C., Rach, S., Neuling, T. & Strüber, D. Transcranial alternating current stimulation: a review of the underlying mechanisms and modulation of cognitive processes. *Frontiers in Human Neuroscience* **7**, 279 (2013).
8. Marshall, L., Helgadóttir, H., Mölle, M. & Born, J. Boosting slow oscillations during sleep potentiates memory. *Nature* **444**, 610–613 (2006).
9. Berenyi, A., Belluscio, M., Mao, D. & Buzsáki, G. Closed-Loop Control of Epilepsy by Transcranial Electrical Stimulation. *Science* **337**, 735–737 (2012).
10. Fröhlich, F. & McCormick, D. A. Endogenous Electric Fields May Guide Neocortical Network Activity. *Neuron* **67**, 129–143 (2010).
11. Anastassiou, C. A., Perin, R., Markram, H. & Koch, C. Ephaptic coupling of cortical neurons. *Nature Neuroscience* **14**, 217–224 (2011).
12. Fröhlich, F. Experiments and models of cortical oscillations as a target for noninvasive brain stimulation. *Progress in Brain Research* **222**, 41–73 (2015).
13. Ozen, S. *et al.* Transcranial Electric Stimulation Entrain Cortical Neuronal Populations in Rats. *Journal of Neuroscience* **30**, 11476–11485 (2010).
14. Alagapan, S. *et al.* Modulation of Cortical Oscillations by Low-Frequency Direct Cortical Stimulation Is State-Dependent. *PLoS Biology* **14**, 1–21 (2016).
15. Herrmann, C. S., Murray, M. M., Ionta, S., Hutt, A. & Lefebvre, J. Shaping Intrinsic Neural Oscillations with Periodic Stimulation. *The Journal of Neuroscience* **36**, 5328–5337 (2016).
16. Brunel, N. Dynamics of sparsely connected networks of excitatory and inhibitory spiking neurons. *Journal of Computational Neuroscience* **8**, 183–208 (2000).
17. Spiegler, A., Kiebel, S. J., Atay, F. M. & Knösche, T. R. Bifurcation analysis of neural mass models: Impact of extrinsic inputs and dendritic time constants. *Neuroimage* **52**, 1041–1058 (2010).
18. Molaee-Ardekani, B. *et al.* Effects of transcranial Direct Current Stimulation (tDCS) on cortical activity: A computational modeling study. *Brain Stimulation* **6**, 25–39 (2013).
19. D’Andola, M., Weinert, J. F., Mattia, M. & Sanchez-Vives, M. V. Modulation of slow and fast oscillations by direct current stimulation in the cerebral cortex in vitro. *bioRxiv* **01** (2018).
20. Brunel, N. Phase diagrams of sparsely connected networks of excitatory and inhibitory spiking neurons. *Neurocomputing* **32-33**, 307–312 (2000).
21. Grimbert, F. & Olivier, F. Bifurcation analysis of neural mass equations. *Neural Computation* **18**, 3052–3068 (2006).
22. Deco, G., Jirsa, V. K., Robinson, P. A., Breakspear, M. & Friston, K. The dynamic brain: From spiking neurons to neural masses and cortical fields. *PLoS Computational Biology* **4**, e1000092 (2008).
23. Breakspear, M. Dynamic models of large-scale brain activity. *Nature Neuroscience* **20**, 340–352 (2017).
24. Gu, S. *et al.* Controllability of structural brain networks. *Nature Communications* **6**, 8414 (2015).
25. Muldoon, S. F. *et al.* Stimulation-Based Control of Dynamic Brain Networks. *PLoS Computational Biology* **12** (2016).

26. Augustin, M., Ladenbauer, J., Baumann, F. & Obermayer, K. Low-dimensional spike rate models derived from networks of adaptive integrate-and-fire neurons: comparison and implementation. *PLoS Computational Biology* **13**, e1005545 (2017).
27. Ostojic, S. & Brunel, N. From spiking neuron models to linear-nonlinear models. *PLoS Computational Biology* **7** (2011).
28. Brette, R. & Gerstner, W. Adaptive exponential integrate-and-fire model as an effective description of neuronal activity. *J. Neurophysiol.* **94**, 3637–3642 (2005).
29. Jolivet, R. *et al.* A benchmark test for a quantitative assessment of simple neuron models. *Journal of Neuroscience Methods* **169**, 417–424 (2008).
30. Naud, R., Marcille, N., Clopath, C. & Gerstner, W. Firing patterns in the adaptive exponential integrate-and-fire model. *Biological Cybernetics* **99**, 335–347 (2008).
31. Aspart, F., Ladenbauer, J. & Obermayer, K. Extending Integrate-and-Fire Model Neurons to Account for the Effects of Weak Electric Fields and Input Filtering Mediated by the Dendrite. *PLoS Computational Biology* **12**, 1–29 (2016).
32. Jercog, D. *et al.* UP-DOWN cortical dynamics reflect state transitions in a bistable network. *eLife* **6**, 1–33 (2017).
33. Tartaglia, Elisa M., Brunel, Nicolas, Bistability and up/down state alternations in inhibition-dominated randomly connected networks of LIF neurons. *Scientific Reports* **7**, 1–14 (2017).
34. Radman, T., Ramos, R. L., Brumberg, J. C. & Bikson, M. Role of cortical cell type and morphology in subthreshold and suprathreshold uniform electric field stimulation in vitro. *Brain Stimulation* **2**, 215–228.e3 (2009).
35. Madison, B. Y. D. V. & Nicoll, R. A. Control of the repetitive discharge of rat CA 1 pyramidal neurones in vitro. *J. Physiol.* **354**, 319–331 (1984).
36. Deans, J. K., Powell, A. D. & Jefferys, J. G. Sensitivity of coherent oscillations in rat hippocampus to AC electric fields. *Journal of Physiology* **583**, 555–565 (2007).
37. Ali, M. M., Sellers, K. K. & Frohlich, F. Transcranial Alternating Current Stimulation Modulates Large-Scale Cortical Network Activity by Network Resonance. *Journal of Neuroscience* **33**, 11262–11275 (2013).
38. Huang, Y. *et al.* Measurements and models of electric fields in the in vivo human brain during transcranial electric stimulation. *eLife* **6**, 1–26 (2017).
39. Helfrich, R. *et al.* Entrainment of Brain Oscillations by Transcranial Alternating Current Stimulation. *Current Biology* **24**, 333–339 (2014).
40. Witkowski, M. *et al.* Mapping entrained brain oscillations during transcranial alternating current stimulation (tACS). *Neuroimage* **140**, 89–98 (2016).
41. Hansen, E. C. A., Battaglia, D., Spiegler, A., Deco, G. & Jirsa, V. K. Functional connectivity dynamics: Modeling the switching behavior of the resting state. *Neuroimage* **105**, 525–535 (2015).
42. Betzel, R. F., Gu, S., Medaglia, J. D., Pasqualetti, F. & Bassett, D. S. Optimally controlling the human connectome: the role of network topology. *Scientific Reports* **6** (2016).
43. Holmgren, C., Harkany, T., Svennenfors, B. & Zilberter, Y. Pyramidal cell communication within local networks in layer 2/3 of rat neocortex. *Journal of Physiology* **551**, 139–153 (2003).
44. Laughlin, S. B. & Sejnowski, T. J. Communication in neuronal networks. *Science* **301**, 1870–1874 (2003).
45. Destexhe, A., Rudolph, M. & Paré, D. The high-conductance state of neocortical neurons in vivo. *Nature Reviews Neuroscience* **4**, 739–751 (2003).
46. Fries, P. *et al.* Modulation of Oscillatory Neuronal Synchronization by Selective Visual Attention Modulation of Oscillatory Neuronal Synchronization by Selective Visual Attention. *Science (New York, N.Y.)* **291**, 1560–3 (2001).
47. Wang, X.-j. Neurophysiological and Computational Principles of Cortical Rhythms in Cognition. *Physiological Reviews* 1195–1268 (2010).
48. Williams, S. R. & Stuart, G. J. Dependence of EPSP efficacy on synapse location in neocortical pyramidal neurons. *Science* **295**, 1907–1910 (2002).
49. Brunel, N. What Determines the Frequency of Fast Network Oscillations With Irregular Neural Discharges? I. Synaptic Dynamics and Excitation-Inhibition Balance. *Journal of Neurophysiology* **90**, 415–430 (2003).
50. Hertäg, L., Durstewitz, D. & Brunel, N. Analytical approximations of the firing rate of an adaptive exponential integrate-and-fire neuron in the presence of synaptic noise. *Frontiers in Computational Neuroscience* **8**, 116 (2014).

51. Fourcaud-Trocmé, N., Hansel, D., van Vreeswijk, C. & Brunel, N. How spike generation mechanisms determine the neuronal response to fluctuating inputs. *J. Neurosci.* **23**, 11628–11640 (2003).
52. Richardson, M. J. E. Firing-rate response of linear and nonlinear integrate-and-fire neurons to modulated current-based and conductance-based synaptic drive. *Physical Review E* **76**, 021919 (2007).
53. Ladenbauer, J. *The collective dynamics of adaptive neurons: insights from single cell and network models*. Ph.D. Thesis, Technische Universität Berlin (2015).
54. Nykamp, D. Q. & A, D. T. A population density approach that facilitates large-scale modeling of neural networks: Analysis and an application to orientation tuning. *Journal of Computational Neuroscience* **8**, 19–50 (2000).
55. Renart, A., Brunel, N. & Wang, X.-J. Mean field theory of irregularly spiking neuronal populations and working memory in recurrent cortical networks. In *Computational Neuroscience A Comprehensive Approach*, 431–490 (2004).
56. Richardson, M. J. Effects of synaptic conductance on the voltage distribution and firing rate of spiking neurons. *Physical Review E - Statistical Physics, Plasmas, Fluids, and Related Interdisciplinary Topics* **69**, 8 (2004).
57. Gigante, G., Mattia, M. & Giudice, P. Diverse population-bursting modes of adapting spiking neurons. *Phys. Rev. Lett.* **98**, 1–4 (2007).
58. Movellan, J. R. Tutorial on Stochastic Differential Equations. *MPLab Tutorials* **6** (2011).
59. Womble, M. D. & Moises, H. C. Muscarinic inhibition of M-current and a potassium leak conductance in neurones of the rat basolateral amygdala. *The Journal of Physiology* **457**, 93–114 (1992).
60. Stocker, M. Ca(2+)-activated K+ channels: molecular determinants and function of the SK family. *Nat. Rev. Neurosci.* **5**, 758–770 (2004).
61. Augustin, M., Ladenbauer, J. & Obermayer, K. How adaptation shapes spike rate oscillations in recurrent neuronal networks. *Front. Comput. Neurosci.* **7**, 1–11 (2013).
62. La Camera, G. *et al.* Multiple time scales of temporal response in pyramidal and fast spiking cortical neurons. *J. Neurophysiol.* **96**, 3448–3464 (2006).
63. Lundqvist, M., Compte, A. & Lansner, A. Bistable, irregular firing and population oscillations in a modular attractor memory network. *PLoS Computational Biology* **6**, 1–12 (2010).
64. Welch, P. The use of fast Fourier transform for the estimation of power spectra: a method based on time averaging over short, modified periodograms. *IEEE Transactions On Audio and Electroacoustics* **15**, 70–73 (1967).
65. Jones, E., Oliphant, T., Peterson, P. & Others. SciPy: Open source scientific tools for Python (2001).
66. Kuramoto, Y. *Chemical Oscillations, Waves, and Turbulence* (Courier Corporation, 2003).
67. Stimberg, M., Goodman, D. F. M., Benichoux, V. & Brette, R. Equation-oriented specification of neural models for simulations. *Front. in Neuroinform.* **8**, 1–14 (2014).

## Supplementary Figures

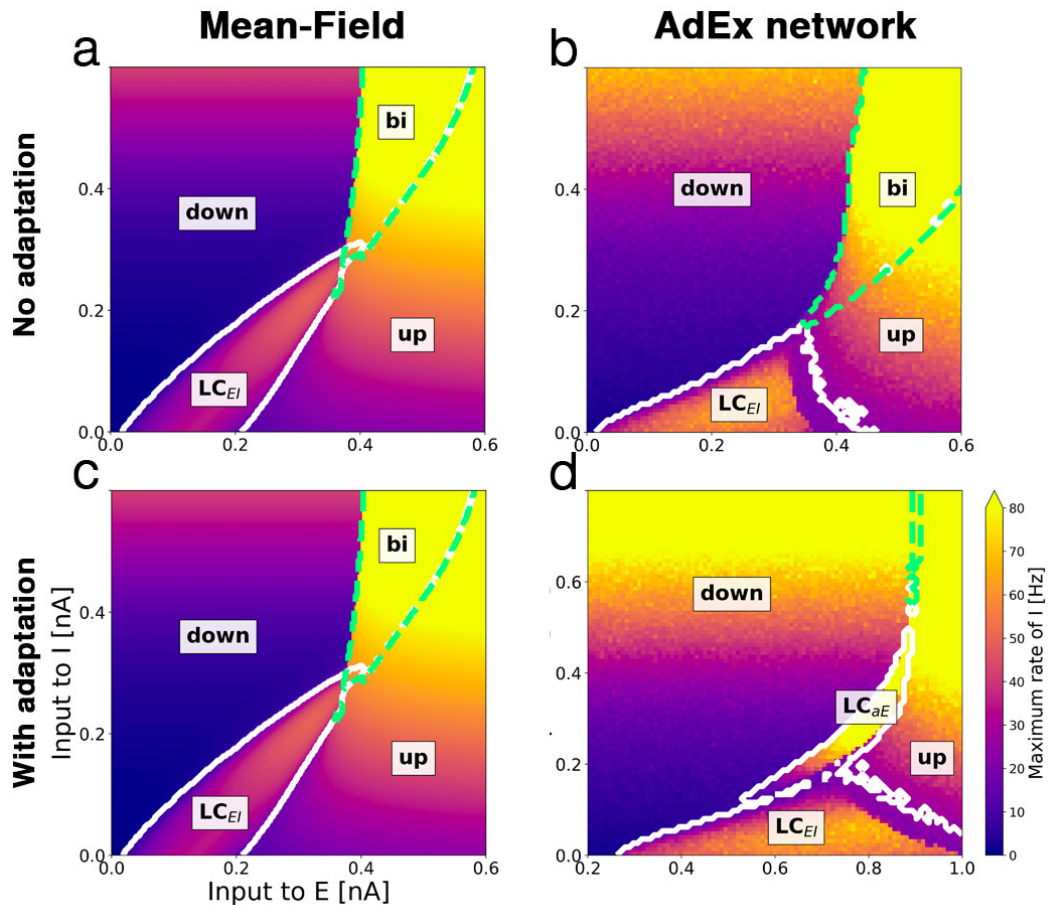


**Figure 9. Bifurcation diagrams with maximum rate of inhibitory population.** (a) Bifurcation diagram of mean-field model without adaptation with *up* and *down*-states, a bistable region *bi* (green dashed contour) and an oscillatory region  $LC_{EI}$  (white solid contour). (b) Diagram of the corresponding AdEx network. (c) Mean-field model with somatic adaptation has a slow oscillatory region  $LC_{aE}$ . (d) Diagram of the corresponding AdEx network. The color indicates the maximum population rate of the inhibitory population (clipped at 80 Hz). All parameters are given in Table 1 in the main manuscript.

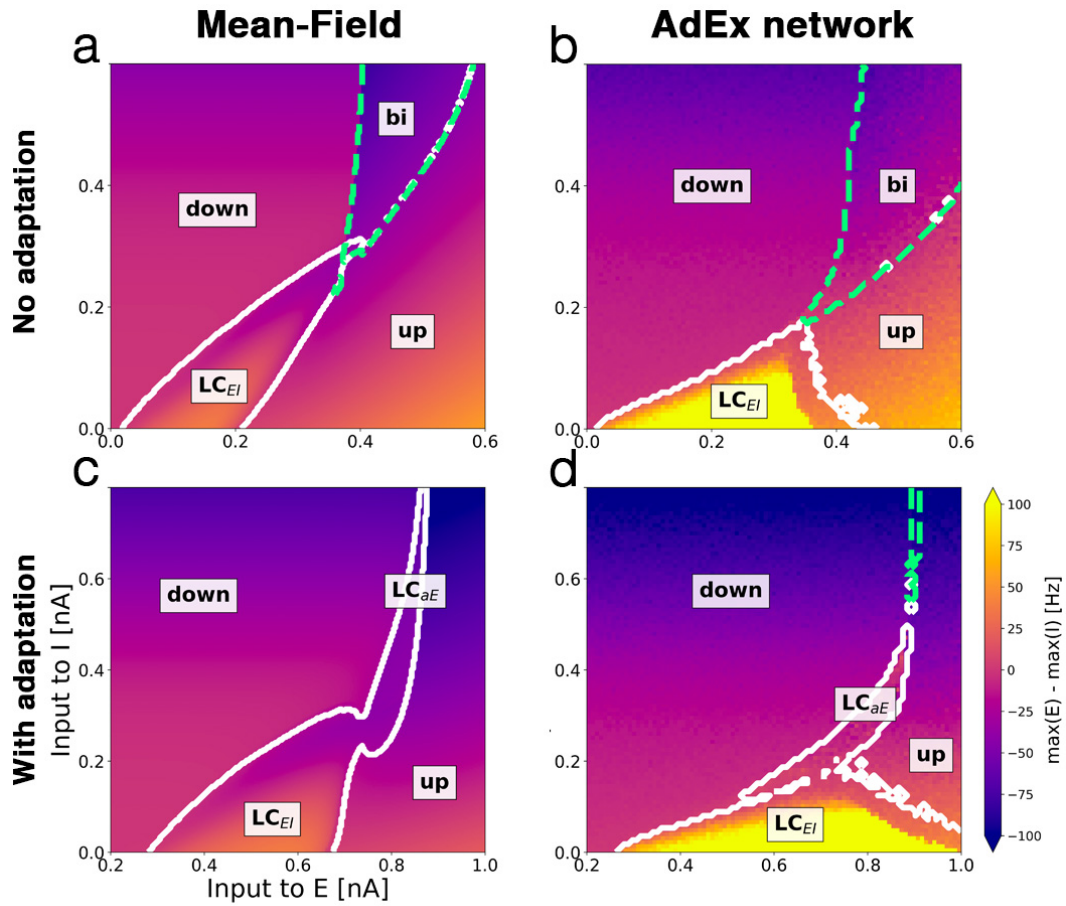


**Figure 10. Bifurcation diagrams depicting the difference of excitatory and inhibitory amplitudes.** (a) Bifurcation diagram of mean-field model without adaptation with *up* and *down*-states, a bistable region *bi* (green dashed contour) and an oscillatory region  $LC_{EI}$  (white solid contour). (b) Diagram of the corresponding AdEx network. (c) Mean-field model with somatic adaptation has a slow oscillatory region  $LC_{aE}$ . (d) Diagram of the corresponding AdEx network. The color indicates the difference of excitatory and inhibitory amplitudes (clipped from -100 Hz to 100 Hz). All parameters are given in Table 1 in the main manuscript.



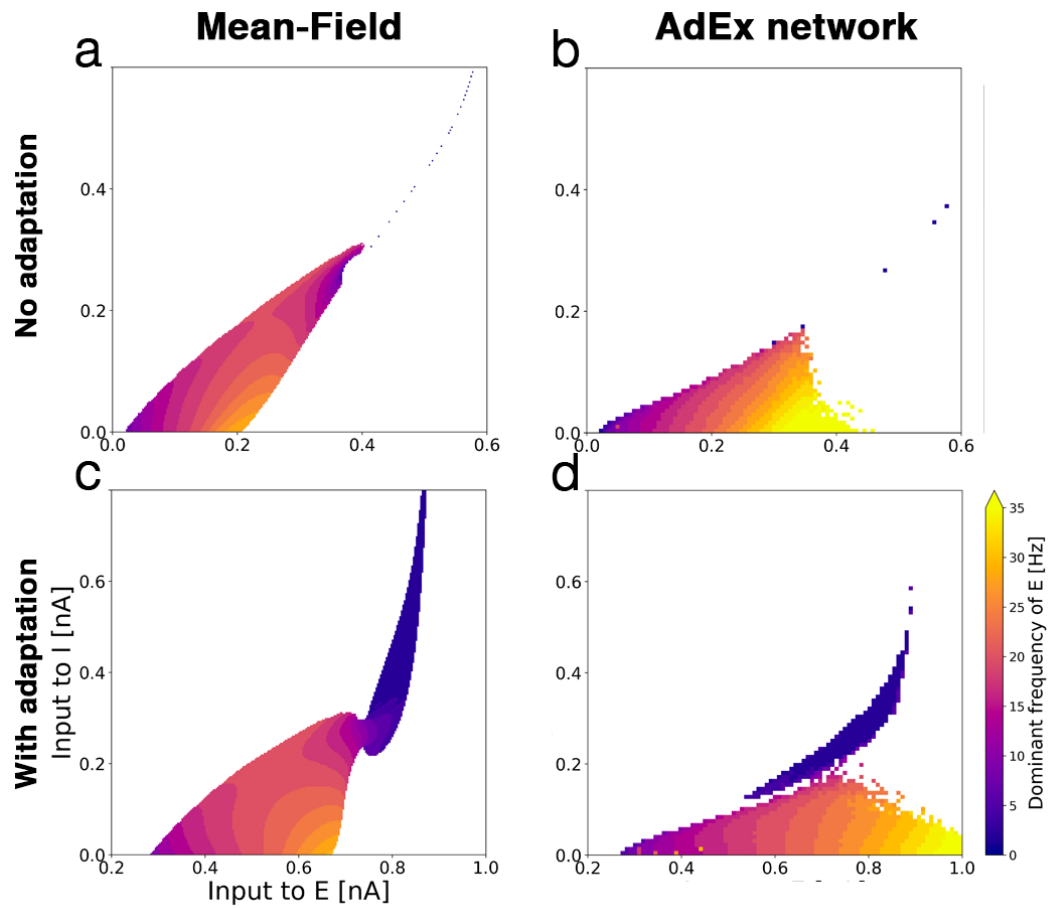


**Figure 11. Bifurcation diagrams with dominant oscillation frequency of the excitatory population.** (a) Bifurcation diagram of mean-field model without adaptation. (b) Diagram of the corresponding AdEx network. (c) Mean-field model with somatic adaptation. (d) Diagram of the corresponding AdEx network. The color indicates the difference of excitatory and inhibitory amplitudes (clipped at 35 Hz). All parameters are given in Table 1 in the main manuscript.

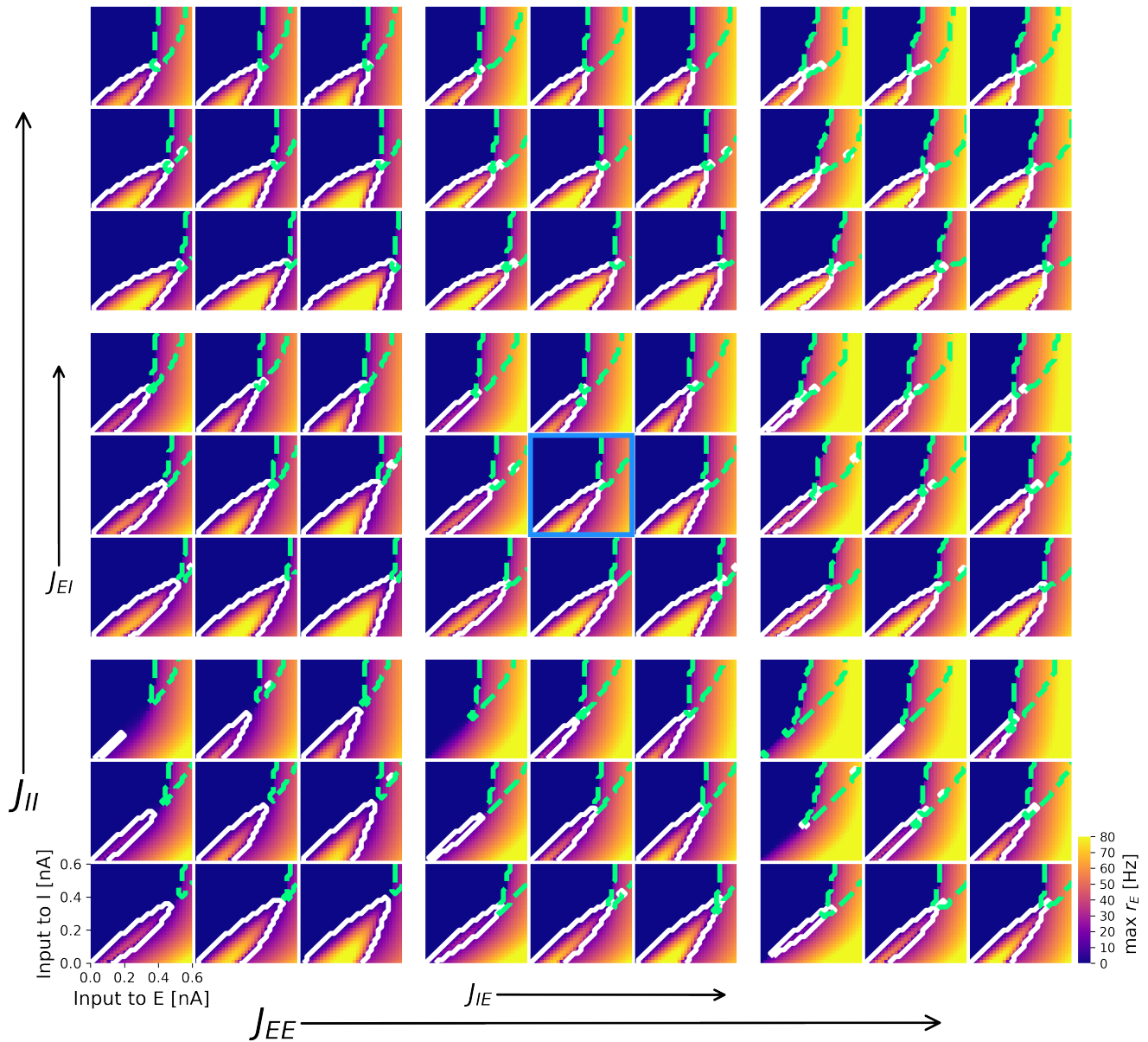


**Figure 12. Bifurcation diagrams of mean-field model for changing coupling strengths.** Stacked bifurcation diagrams depending on the mean input current to populations E and I showing dynamical states for increasing  $J_{EE}$  and  $J_{II}$  (outer axis),  $J_{IE}$  and  $J_{EI}$  (inner axis) by values of 0.5 mV/ms. The middle rows and columns correspond to the default value of the corresponding parameter (see Table 1). White contours are oscillatory areas  $LC_{EI}$ , green dashed contours are bistable regions. The system has no somatic adaptation. Diagram in the middle (blue box) corresponds to bifurcation diagram Fig. 2 a in the main manuscript. All other parameters are given in Table 1 in the main manuscript.